Article

Cell Reports

Cdc42EP3/BORG2 and Septin Network Enables Mechano-transduction and the Emergence of Cancer-Associated Fibroblasts

Graphical Abstract

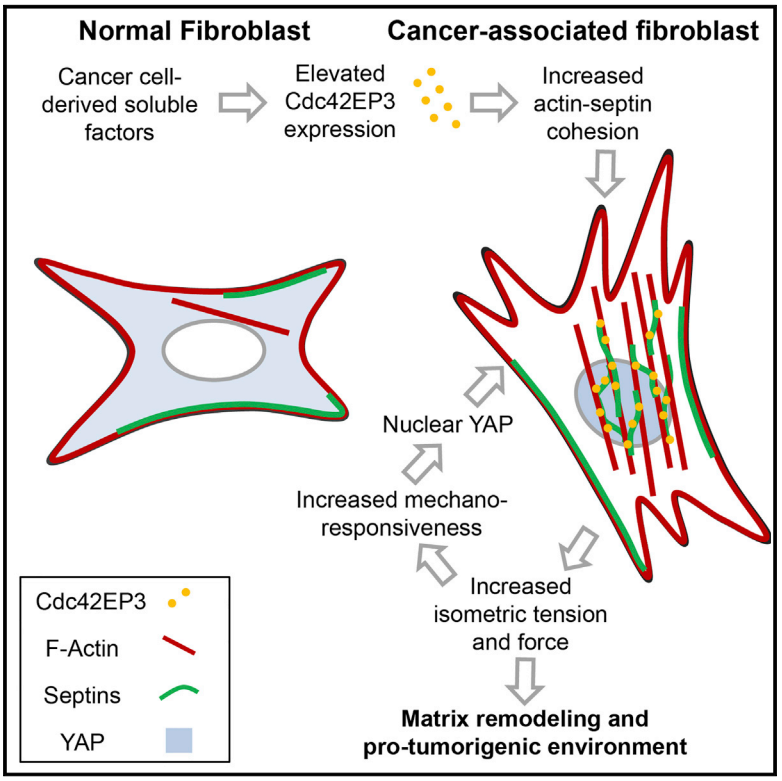

Highlights

- Cdc42EP3-mediated coordination of actin and septin is required for CAF function
- The septin network is changed in CAFs and is required for their function
- Cdc42EP3 enables responses to changes in matrix stiffness
- Upregulation of Cdc42EP3 is required for the activation of normal fibroblasts

Authors

Fernando Calvo, Romana Ranftl, Steven Hooper, ..., Facundo Batista, Guillaume Charras, Erik Sahai

Correspondence

fernando.calvo@icr.ac.uk (F.C.), erik.sahai@crick.ac.uk (E.S.)

In Brief

Calvo et al. identify Cdc42EP3 as a regulator of the pro-tumorigenic functions of cancer-associated fibroblasts. Cdc42EP3 is upregulated during fibroblast activation and coordinates actin and septin rearrangements that are required for mechanotransduction and CAF functions.

Calvo et al., 2015, Cell Reports *13*, 2699–2714
December 29, 2015
http://dx.doi.org/10.1016/j.celrep.2015.11.052

Cell Reports
Article

Cdc42EP3/BORG2 and Septin Network Enables Mechano-transduction and the Emergence of Cancer-Associated Fibroblasts

Fernando Calvo,[1,2,*] Romana Ranftl,[2] Steven Hooper,[1] Aaron J. Farrugia,[2] Emad Moeendarbary,[3,4] Andreas Bruckbauer,[5] Facundo Batista,[5] Guillaume Charras,[3,6] and Erik Sahai[1,*]
[1]Tumour Cell Biology Laboratory, Francis Crick Institute, 44 Lincoln's Inn Fields, London WC2A 3LY, UK
[2]Tumour Microenvironment Team, Division of Cancer Biology, Institute of Cancer Research, 237 Fulham Road, London SW2 6JB, UK
[3]London Centre for Nanotechnology, University College London, London WC1H 0AH, UK
[4]Department of Biological Engineering, Massachusetts Institute of Technology, Cambridge, MA 02142, USA
[5]Lymphocyte Interaction Laboratory, Cancer Research UK London Research Institute, 44 Lincoln's Inn Fields, London WC2A 3LY, UK
[6]Department of Cell and Developmental Biology, University College London, London WC1E 6BT, UK
*Correspondence: fernando.calvo@icr.ac.uk (F.C.), erik.sahai@crick.ac.uk (E.S.)
http://dx.doi.org/10.1016/j.celrep.2015.11.052

SUMMARY

Cancer-associated fibroblasts (CAFs) are non-cancerous cells found in solid tumors that remodel the tumor matrix and promote cancer invasion and angiogenesis. Here, we demonstrate that Cdc42EP3/BORG2 is required for the matrix remodeling, invasion, angiogenesis, and tumor-growth-promoting abilities of CAFs. Cdc42EP3 functions by coordinating the actin and septin networks. Furthermore, depletion of SEPT2 has similar effects to those of loss of Cdc42EP3, indicating a role for the septin network in the tumor stroma. Cdc42EP3 is upregulated early in fibroblast activation and precedes the emergence of the highly contractile phenotype characteristic of CAFs. Depletion of Cdc42EP3 in normal fibroblasts prevents their activation by cancer cells. We propose that Cdc42EP3 sensitizes fibroblasts to further cues—in particular, those activating actomyosin contractility—and thereby enables the generation of the pathological activated fibroblast state.

INTRODUCTION

Non-cancerous cells and matricellular molecules within the tumor, collectively defined as the tumor microenvironment (Bhowmick and Moses, 2005; Calvo and Sahai, 2011; Joyce and Pollard, 2009), participate in many hallmarks of cancer (Hanahan and Coussens, 2012). Cancer-associated fibroblasts (CAFs) can provide chemical and physical cues that favor tumor aggressiveness and dissemination (Kalluri and Zeisberg, 2006; Karnoub et al., 2007). CAF-dependent matrix remodeling can lead to the generation of tracks through the extracellular matrix (ECM) that enable subsequent cancer cell invasion (Gaggioli et al., 2007). As a result of increased deposition and remodeling of the ECM by CAFs, most solid tumors are characterized by elevated cellular and tissue tension, and enhanced stiffness (DuFort et al., 2011; Levental et al., 2009; Paszek et al., 2005). These altered physical properties can promote malignancy by enhancing cancer cell growth, survival, and migration (DuFort et al., 2011). CAFs also produce soluble factors that can promote tumorigenesis (Öhlund et al., 2014). Thus, targeting CAFs represents a possibility for therapeutic intervention.

Changes in the actin cytoskeleton, including increased actin stress fibers, αSMA expression, and stronger focal adhesions, is a feature of CAFs (Calvo et al., 2013; Kalluri and Zeisberg, 2006; Öhlund et al., 2014; Sandbo et al., 2011; Xing et al., 2010). Increased actomyosin contractility also leads to activation of the transcriptional regulator YAP1 that is critical for the CAF phenotype (Calvo et al., 2013). Much less is known about alterations to other cytoskeletal networks. Septins are a large conserved family of GTP-binding proteins that participate in cell division, cytoskeletal organization, vesicular transport, cell polarity, and membrane remodeling (Mostowy and Cossart, 2012; Weirich et al., 2008). SEPT2, SEPT6, and SEPT7 can assemble into hetero-oligomeric complexes and higher-order structures, including filaments and rings (Sirajuddin et al., 2007). The adaptor protein Anillin (ANLN) controls actin-septin coordination during cytokinesis, whereas unknown factors mediate this process during interphase (Kinoshita et al., 2002). BORG family proteins, such as Cdc42EP3 and Cdc42EP5, are potential candidates to fulfill this role. These proteins bind active Cdc42 (Bahou et al., 1992; Joberty et al., 1999) and SEPT2, 6, and 7 (Joberty et al., 2001). Overexpression of Cdc42EP3 in fibroblasts can induce the formation of pseudopodia and F-actin-containing structures (Hirsch et al., 2001), while Cdc42EP5 can regulate septin organization within the cell (Joberty et al., 2001; Sheffield et al., 2003). However, the role of BORG proteins in the tumor microenvironment is not well understood. Here, we examine the role of Cdc42EP3/BORG2 and septins in regulating CAF emergence, maintenance, and functions linked to essential rearrangements in the actin and septin network.

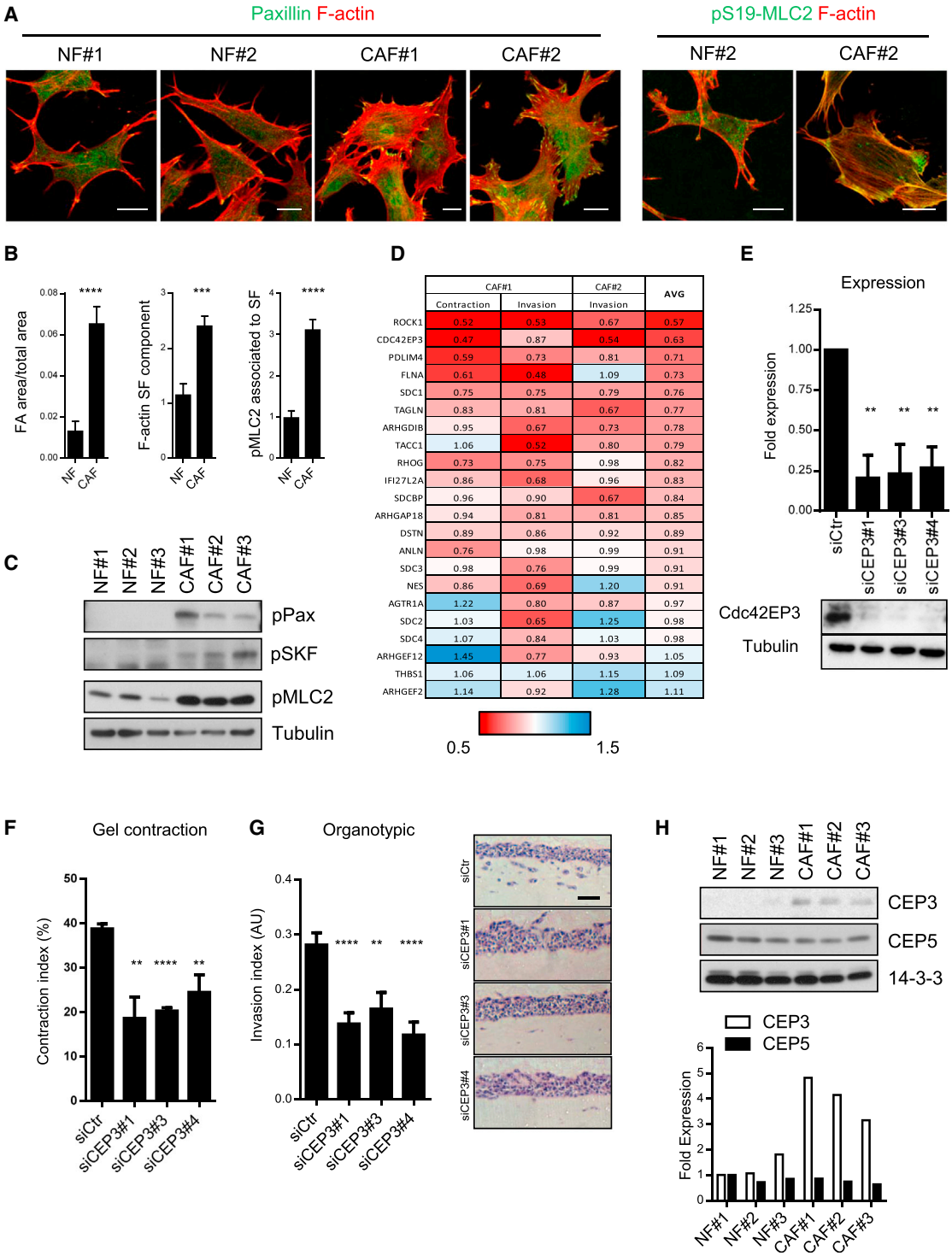

Figure 1. Identification of Cdc42EP3 as a Key Regulator of CAF Functions

(A) The left panels show images of F-actin (red) and paxillin (green) staining in NF#1, NF#2, CAF#1, and CAF#2. The right panels show images of F-actin (red) and pS19-MLC2 (green) staining in NF#2 and CAF#2. Scale bars represent 20 μm.

(B) Histograms show focal adhesion (FA) area normalized to total cell area (left graph), an F-actin stress fibers (SF) component (middle graph), and pMLC2 associated to SF (right graph) of NF and CAF cells. Bars represent mean ± SEM. FA measurements, n = 16; measurements were performed on NF#1 and NF#2 (NF) and CAF#1 and CAF#2 (CAF). F-actin and pMLC2 measurements, n = 12 for NF and n = 15 for CAF; measurements were performed on NF#1 and CAF#1.

(legend continued on next page)

RESULTS

Identification of Cdc42EP3 as a Regulator of CAF Functions

To learn about the role of the cytoskeleton in CAFs, we compared its organization in normal fibroblasts (NFs) and CAFs from the MMTV-PyMT mammary tumor model (Calvo et al., 2013). In NFs, F-actin was mainly at the cell cortex and only small focal adhesions were present (Figure 1A; quantification in Figure 1B). In contrast, CAFs had enhanced F-actin stress fibers containing active pS19 myosin light chain 2 (MLC2; phosphorylation on S19 is the major positive regulatory mechanism of myosin activity in non-muscle cells) and abundant paxillin-positive focal adhesions (Figure 1A; quantification in Figure 1B). We confirmed the elevated levels of pS19-MLC2 in CAFs by western blotting (Figure 1C) and also observed elevated levels of active Src-family kinases and increased phosphorylation of paxillin on the FAK and Src-family kinase site, Y118 (Figure 1C) (Deakin and Turner, 2008).

We selected 21 cytoskeletal components that are highly expressed in CAFs compared to NFs based on microarray data (Calvo et al., 2013) and depleted them in CAFs. Following small interfering RNA (siRNA) transfection, the ability of CAF#1 to contract collagen gels and promote the invasion of breast cancer cells in ''organotypic'' assays was determined. Invasion assays were also performed using CAF#2. Figure 1D shows the effect of gene depletion in each assay, together with a combined metric of ''CAF functionality'' derived by averaging the individual assay results. Depletion of *Cdc42ep3* reduced CAF function to a similar extent as targeting *Rock1* (Figure 1D), a known regulator of CAF function that was used as a positive control (Gaggioli et al., 2007). Depletion of Cdc42EP3 with three independent siRNA led to reduced ECM remodeling by CAFs (Figures 1E and 1F, confirmed in CAF#2; Figure S1A). There was also a significant reduction in the cancer cell invasion promoting abilities of CAF#1 and CAF#2 after Cdc42EP3 depletion (Figures 1G and S1A). Similar results were obtained in human-patient-derived CAFs (Figures S1B–S1D). Depletion of Cdc42EP3 did not affect the expression of the CAF markers αSMA and FAP (Figure S1E).

Cdc42ep3 encodes a protein of the BORG family of Cdc42 effectors (Joberty et al., 1999). We confirmed that Cdc42EP3 levels were upregulated in three different CAFs when compared to NFs (Figure 1H), whereas levels of other BORG members were unchanged (Figures 1H and S1F). Analysis of expression levels of BORG genes in patient datasets (Finak et al., 2008; Karnoub et al., 2007) revealed that *CDC42EP3* was consistently upregulated in the stromal compartment of human breast carcinoma compared to normal tissue samples (Figure S1G). These analyses led us to focus on Cdc42EP3 in CAFs.

Altered Septin Networks Are a Feature of CAFs

BORG proteins can regulate the actin and septin cytoskeleton (Joberty et al., 1999, 2001). We therefore investigated the septin network in NFs and CAFs. SEPT2 and SEPT7 formed more extensive networks in CAFs (Figure 2A; quantification in Figure S2A) that generally co-aligned with actin stress fibers (Figure S2B). This was confirmed using a biochemical method based on fractionation of detergent insoluble cytoskeletal components (Posern et al., 2002). In NFs the amount of actin present in the insoluble fraction was low (Figures 2B and S2C). This increased greatly in all four CAFs examined. Importantly, there was a similar shift of both SEPT2 and SEPT7 into the insoluble fraction in CAF#1–4 (Figures 2B and S2C). Time-lapse imaging of CAFs revealed that SEPT2 was highly dynamic, with SEPT2 puncta moving on and off actin stress fibers (Figure S2D; Movie S1). In contrast, SEPT2 localization and dynamics did not show a clear relationship to actin in NFs (Figure S2D; Movie S2). This was reflected in the lower co-localization coefficient of the Lifeact and SEPT2-GFP probes in NFs (Figures S2E and S2F demonstrate that GFP does not co-localize with F-actin). Structured illumination microscopy (SIM) revealed that SEPT2-GFP was present along actin stress fibers, but not always exactly coincident with them (Figure 2C, white arrows). Furthermore, there were wavy filaments that occasionally connected nearby stress fibers (Figure 2C, green arrows). We hypothesized that Cdc42EP3 may coordinate the actin and septin networks. Endogenous Cdc42EP3 partially co-localized with actin stress fibers in CAFs (Figure 2D). Further, SIM revealed that Cdc42EP3-GFP forms an intricate filamentous network in CAFs (Figure 2E). Similar to the SEPT2 network, the Cdc42EP3 network is clearly aligned with, but not exactly coincident with, F-actin (Figure 2E). It often formed filaments close to, or wrapped around, actin stress fibers (Figure 2E, white arrows), while other filaments presented a wavy pattern and did not co-align with F-actin (Figure 2E, yellow arrows). Time-lapse imaging showed that Cdc42EP3 moved both between and along stress fibers, in a manner similar to SEPT2 (Movies S3 and S4). Triple labeling of F-actin, SEPT2-Cherry, and Cdc42EP3-GFP revealed that Cdc42EP3 co-localized with

(C) Western blot showing pY118-paxillin (pPax), pY416-Src (pSFK), and pS19-MLC2 (pMLC2) in three sets of NF and CAFs (NF#1, NF#2, NF#3, CAF#1, CAF#2, and CAF#3). A tubulin blot is also shown.

(D) RNAi-based loss-of-function screen in CAFs. The indicated genes (left column) were knocked down by smart-pool siRNA, and the functional outcomes were evaluated in gel contraction (CAF#1) and organotypic invasion assays (CAF#1 and CAF#2). The values indicate the fold activity normalized to control siRNA-transfected CAFs for each experiment (red is low; blue is high). Genes are ranked on their average score (right column).

(E) Western blot and quantification showing Cdc42EP3 and tubulin expression in CAF#1 after transfection with control and three different Cdc42EP3 siRNA (siCEP3). Bars represent mean ± SEM (n = 4).

(F) Histogram shows gel contraction by CAF#1 following transfection with control or three different Cdc42EP3 siRNA (siCEP3). Bars represent mean ± SEM (n = 3).

(G) Images and quantification of 4T1 invasion when co-cultured with CAF#1 transfected with control or three single Cdc42EP3 siRNA (siCEP3). Bars represent mean ± SEM (n = 14 organotypic assays assessed over three experiments). Scale bar, 50 μm.

(H) Western blots showing Cdc42EP3, Cdc42EP5, and 14-3-3 levels in three sets of NF and CAFs (NF#1–3, CAF#1–3). The chart shows Cdc42EP3 and Cdc42EP5 fold expression (normalized to 14-3-3).

See also Figure S1.

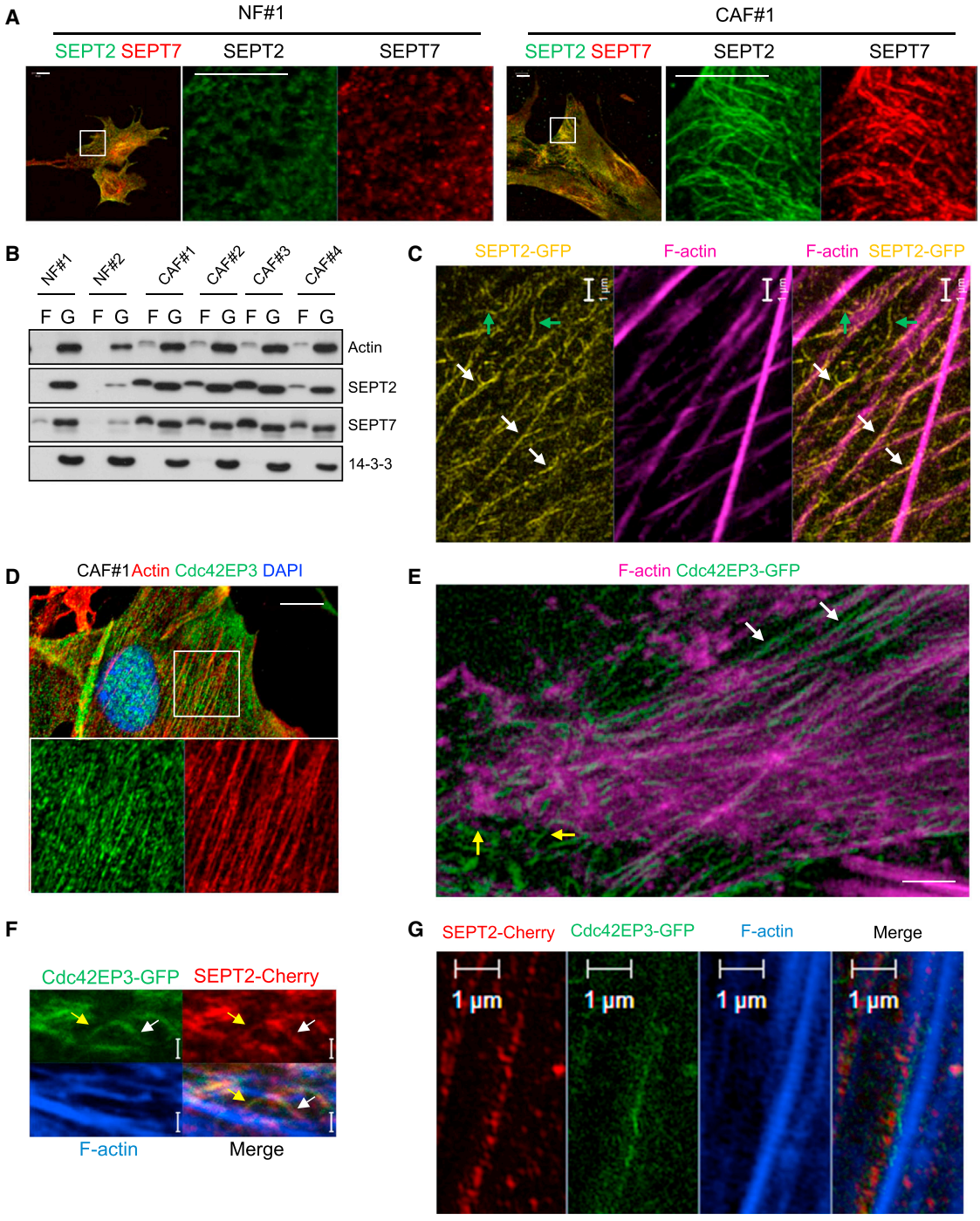

Figure 2. CAFs Have Enhanced Actin and Septin Cytoskeletal Networks

(A) Panels show SEPT2 (green) and SEPT7 (red) staining in NF#1 and CAF#1. Zoom areas are shown for each channel and cell type. Scale bars represent 10 μm. See Figure S2A for quantification.

(B) Western blot showing the fibrillar (F) and soluble (G) content of actin, SEPT2, and SEPT7 in two NF lines (NF#1-2) and four CAF lines (CAF#1-4). A 14-3-3 blot is also shown as an internal cytosolic control. See Figure S2C for quantification.

(C) Representative SIM images of SEPT2-GFP (yellow) and F-actin (magenta) staining in CAF#1. White arrows indicate SEPT2-GFP filaments along actin stress fibers. The green arrows indicate SEPT2-GFP filaments connecting nearby stress fibers. Scale bars represent 1 μm.

(D) Panels show actin (red), endogenous Cdc42EP3 (green), and DAPI (blue) staining of CAF#1. Cells were fixed using methanol. Zoom-up area showing actin and Cdc42EP3 is shown. Bar represents 10 μm.

(legend continued on next page)

SEPT2 filaments (Figure 2F). These filaments exhibited a partial overlap with F-actin stress fibers (Figure 2F, white arrows), but also formed connections between actin fibers (Figure 2F, yellow arrows). Further, SIM imaging revealed that Cdc42EP3 could localize between F-actin fibers and SEPT2 filaments (Figure 2G). Together, these data suggest that Cdc42EP3 links the actin and septin networks.

Depletion of Cdc42EP3 in CAFs resulted in the loss of actin stress fibers and reduced pS19-MLC2 staining (Figure 3A; quantification in Figure S3A). Moreover, the network of SEPT2 and SEPT7 fibers was also disrupted upon Cdc42EP3 depletion (Figure 3B; quantification in Figure S3B, confirmed with two siRNA in Figure S3C). Fractionation confirmed significant reductions in filamentous insoluble levels of F-actin, SEPT2, and SEPT7 in Cdc42EP3-depleted CAFs (Figures 3C and S3D); the total levels of actin, SEPT2, and SEPT7 were unaltered (Figure S3E). These changes were associated with significantly reduced CAF cellular stiffness (Figure 3D).

Gain-of-function experiments demonstrated that overexpression of Cdc42EP3 in NFs was sufficient to induce actin, SEPT2, and SEPT7 polymerization (Figure 3E). The ability of Cdc42EP3 to bind both septins (Joberty et al., 1999, 2001) and the data in Figure S3I showing a direct interaction with F-actin suggest that it may act as a "molecular glue" linking the two networks. To explore this idea, we generated Cdc42EP3 mutants defective in interaction with septins, F-actin, or Cdc42 (Figures S3F–S3H). We mutated key residues in the septin-binding BD3 domain (Cdc42EP3 GPS-AAA mutant [Joberty et al., 1999, 2001]) and the CRIB domain (Cdc42EP3 IS-AA mutant) (Figure S3G). To generate a putative actin-binding defective mutant, we mutated the amino acids KLP in positions 139–141 (Figure S3H). These residues are within a region of the protein with high homology to the actin bundling region of ANLN (Field and Alberts, 1995) and the actin-binding head piece of villin (Friederich et al., 1992). Immunoprecipitation analyses indicated that the GPS mutant of Cdc42EP3 still interacted with actin but had reduced binding to SEPT2 (Figure S3J). On the other hand, Cdc42EP3 KLP-AAA did not interact with actin but maintained the SEPT2 and SEPT7 binding abilities. Unfortunately, the CRIB domain mutant of Cdc42EP3 (Cdc42EP3 IS-AA) was also defective in interaction with actin; because it did not represent a specific loss of function, we excluded this mutant from further analysis.

We assessed the function of these Cdc42EP3 mutants in NFs, which have low Cdc42EP3 expression and relatively low F-actin and filamentous septin levels (Figures 2A and S2B). Overexpression of wild-type Cdc42EP3 led to prominent SEPT2 and SEPT7 filaments (Figure 3F with quantification in Figure 3H) and actin stress fibers (Figures 3G and 3H). As previously observed in CAFs (Figure 2E), wild-type Cdc42EP3-GFP in NFs formed filamentous structures that co-aligned with septin filaments and actin fibers (Figures 3F and 3G, with quantification in Figure 3H). Neither the GPS nor KLP mutant of Cdc42EP3 could induce the formation of actin or septin fibers (Figures 3F–3H). Further, the localization of both mutants was largely diffuse. These results indicate that Cdc42EP3 needs to directly bind both F-actin and septins to drive both networks into a filamentous state.

The Septin Cytoskeleton Is Required for CAF Functions

To test the role of septins in CAFs, we disrupted the septin network using siRNA-targeting SEPT2. Depletion of SEPT2 led to a loss of actomyosin stress fibers (Figure 4A) and fewer paxillin-containing focal adhesions (Figure 4B). This phenotype was very similar to that observed following Cdc42EP3 depletion or DIAPH1&3 depletion, which is known to block stress fiber formation (Narumiya et al., 2009). Western blotting for pS19-MLC2, active Src-family kinases, and pY118-paxillin confirmed the altered state of the actomyosin cytoskeleton and focal adhesions (Figure 4C). Biochemical fractionation revealed that depletion of either SEPT2 or SEPT7 led to a significant reduction in the level of F-actin in CAFs (Figure 4D). These data establish the inter-relationship of these two networks in CAFs. Next, we investigated the functional importance of the septin network in CAFs. Figure 4E shows that depletion of SEPT2 or SEPT7 significantly reduced the ability of CAF#1 to contract collagen-rich gels (confirmed in other CAFs in Figure S4A). The requirement for both Cdc42EP3 and SEPT2 for effective ECM remodeling was confirmed by staining for the deposition of fibrillar fibronectin and quantification of DQ-collagen I proteolysis (Figures S4B and S4C). Figure 4F further shows that the reduced ECM remodeling was associated with lower matrix stiffness. Moreover, the ability of CAFs to promote cancer cell invasion was reduced following SEPT2 or SEPT7 depletion (Figure 4G; confirmed in other CAFs in Figure S4D).

Next, we sought to test the role of Cdc42EP3 and septins in vivo. CAFs were injected in Matrigel plugs, and matrix remodeling was assessed after 7 days. Control siRNA-transfected CAFs organized collagen into thick bundles that could be visualized by second harmonic imaging and generated elastin fibers that could be detected by their autofluorescent properties (Figure S4E). Depletion of either Cdc42EP3 or SEPT2 greatly reduced the formation of thick collagen bundles and elastin fibers in vivo (Figures 4H and S4F). These data establish that Cdc42EP3 and septins are important for the matrix remodeling and invasion-promoting abilities of CAFs.

(E) Representative SIM image of F-actin (magenta) and Cdc42EP3-GFP (green) in CAF#1. Bar represents 1 μm. White arrows indicate Cdc42EP3-GFP filaments associated to actin stress fibers. Yellow arrows indicate Cdc42EP3-GFP wavy filaments that do not co-align with F-actin.

(F) Single channel and merged confocal images of SEPT2-Cherry (red), Cdc42EP3-GFP (green), and F-actin (blue) in CAF#1. White arrows indicate SEPT2- and Cdc42EP3-containing filaments that co-align with F-actin. Yellow arrows indicate SEPT2- and Cdc42EP3-containing filaments that interconnect F-actin cables. Scale bar represents 1 μm.

(G) Representative single channel and merged SIM images of SEPT2-Cherry (red), Cdc42EP3-GFP (green), and F-actin (blue) in CAF#1. Scale bars represent 1 μm.

See also Figure S2 and Movies S1, S2, S3, and S4.

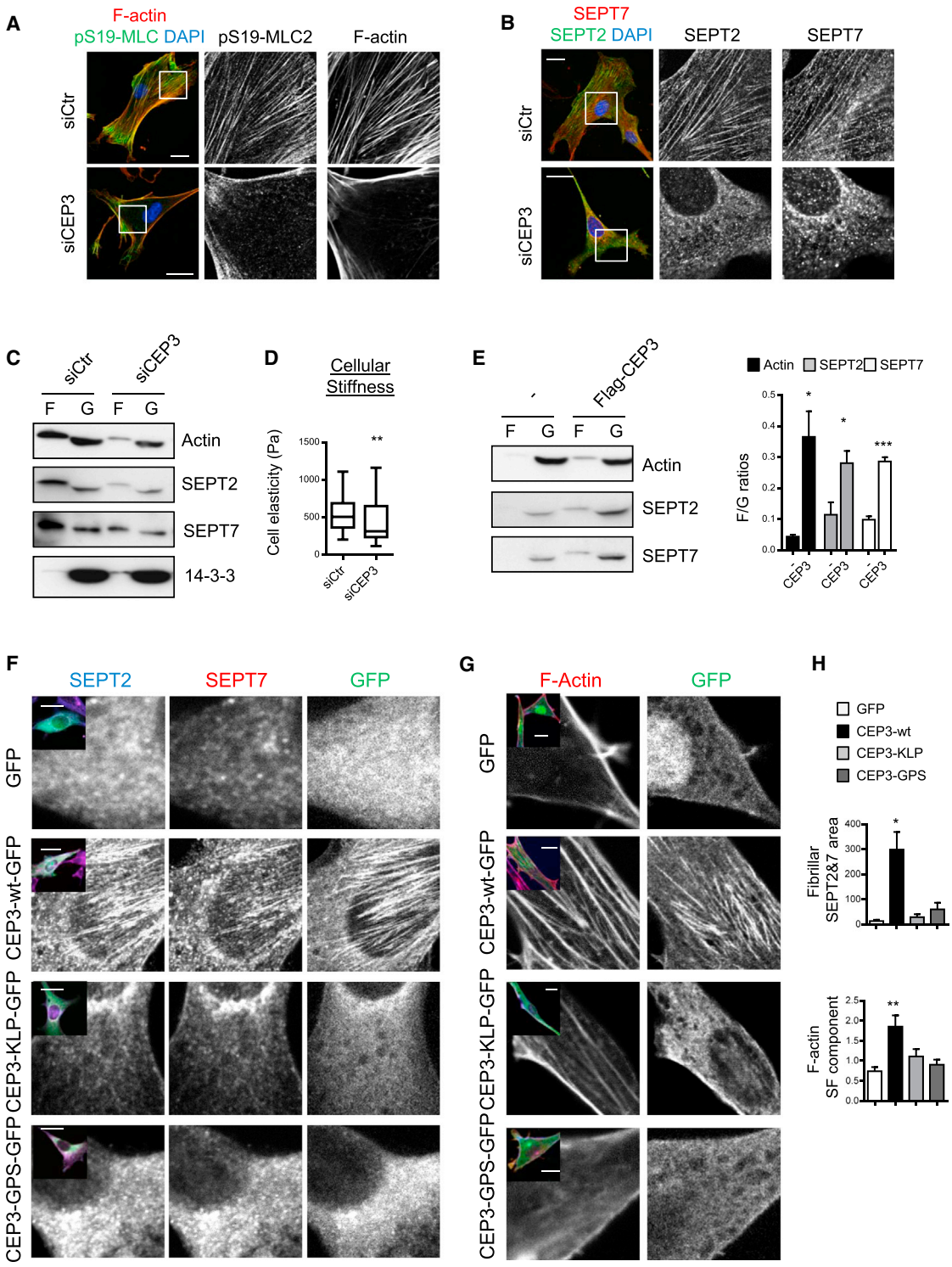

Figure 3. Cdc42EP3 Regulates the Actin and Septin Fibrillar Networks

(A) Images show pS19-MLC2 (green), F-actin (red), and DAPI (blue) staining of CAF#1 following control and Cdc42EP3 siRNA (siCEP3, smart pool). The grayscale panels show individual channel magnifications of the indicated areas. Scale bars, 25 μm. See Figure S3A for quantification.

(B) Images show SEPT2 (green), SEPT7 (red), and DAPI (blue) staining of CAF#1 following control and Cdc42EP3 siRNA (siCEP3, smart pool). The grayscale panels show individual channel magnifications of the indicated areas. Scale bars, 25 μm. See Figure S3B for quantification.

(legend continued on next page)

CAFs Require Cdc42EP3 and SEPT2 to Promote Angiogenesis and Tumor Growth

We hypothesized that Cdc42EP3 might also be required for other functions of CAFs besides matrix remodeling. In particular, we focused on angiogenesis and tumor growth. qRT-PCR analysis revealed that Cdc42EP3 is required in CAFs for the expression of the key angiogenic factor, *Vegfa*, and several other genes implicated in angiogenesis, including *Vegfc*, *Tgfb1*, and *Tgfb2* (Figures 5A and S5A). The expression of other factors involved in tumor-stroma crosstalk was not changed following Cdc42EP3 depletion, or in the case of *Vegfb*, *Tgfb3*, and *Ccl2*, modestly increased (Figure S5A). Consistent with the qRT-PCR data, secreted VEGF-A was reduced in CAFs depleted of Cdc42EP3 or SEPT2 (Figure 5B). We tested the ability of CAFs to drive angiogenesis in vivo. Fibroblasts were injected in Matrigel plugs and the extent of angiogenesis evaluated a week later by endomucin staining. Depletion of Cdc42EP3 or SEPT2 dramatically reduced the angiogenic potential of CAFs in vivo (Figures 5C and 5D). To test whether the defective matrix remodeling and angiogenic activity of CAFs lacking Cdc42EP3 might influence tumor growth, we established CAFs that were stably depleted for Cdc42EP3 using two different small hairpin RNA (shRNA) sequences (Figure S5B). These CAFs, or the appropriate control CAFs, were then "admixed" with PyMT breast cancer cells and injected orthotopically in immune-competent FVB mice. Figure 5E shows that tumors containing Cdc42EP3-depleted CAFs were smaller than those tumors with control CAFs. Depletion of Cdc42EP3 in CAFs was also associated with longer survival (Figure 5F). Histological analysis revealed that αSMA-positive cells were visible in both control and Cdc42EP3-depleted tumors (Figure 5G). More interestingly, tumors containing Cdc42EP3-depleted CAFs tended to grow as a viable rim surrounding a necrotic core (visible in the lower magnification images in Figure 5H). This was correlated with reduced blood vessel density in the interior of the tumors, although similar numbers of vessels were present at the margins.

Cdc42EP3 Is Required for Mechano-transduction and YAP Activation

Cdc42EP3 and SEPT2 are important for regulation of the actomyosin cytoskeleton and paxillin phosphorylation (Figures 4A–4C). As these events are responsive to the mechanical properties of the substratum (DuFort et al., 2011), we hypothesized that Cdc42EP3 and septins may be required for responses to changes in matrix stiffness. Figure 6A shows that GFP-SEPT2 forms fibrillar structures within the cell body in CAFs plated on relatively stiff 12 kPa substrates (Figure 2). However, when the same CAFs are plated on a soft 500 Pa substrate, the distribution of SEPT2 was cortical and fibrillar structures were absent. NFs fail to form SEPT2 fibers in the cell body on both 500 Pa and 12 kPa substrates (Figure 6A). Further, we noted that the localization of Cdc42EP3 in CAFs changed depending on substrate stiffness: it was diffuse on soft substrates and formed fibrillar structures on stiff matrices (Figure S6). These data demonstrate that septin network organization changes in response to substrate stiffness in CAFs, which express high levels of Cdc42EP3.

To test if Cdc42EP3 was causally implicated in the cytoskeletal changes, we undertook a series of gain- and loss-of-function experiments. We observed that, in contrast to control NFs, NFs overexpressing Cdc42EP3 had increased actin stress fibers and focal adhesions on 12 kPa substrates (Figure 6B). We additionally investigated the activity of the mechano-responsive transcriptional co-activator YAP (Calvo et al., 2013; Dupont et al., 2011). Figure 6C shows that Cdc42EP3 overexpression increases the nuclear localization of YAP (quantification in Figure 6D) and leads to a dose-dependent increase in the mRNA levels of two YAP target genes in NFs, *Ctgf*, and *Ankrd1* (Figure 6E). CAFs are highly mechano-responsive; they have few stress fibers or focal adhesions and cytoplasmic YAP on 500 Pa matrices, but on 12 kPa matrices, they have nuclear YAP and form extensive stress fibers and paxillin-containing focal adhesions. In the absence of Cdc42EP3 or SEPT2, these mechano-induced changes do not occur (Figures 6F–6H). We confirmed the reduction in YAP transcriptional activation by measuring *Ankrd1* and *Ctgf* mRNA (Figures 6I). Together, these data show that Cdc42EP3 and the septin network are required for CAFs to respond to changes in matrix stiffness and activation of the mechano-responsive transcriptional regulator YAP.

Cdc42EP3 Is Induced and Required Early in Fibroblast Activation

To explore the chronology of Cdc42EP3 upregulation during the transition from NF to CAF, we evaluated different stages of MMTV-PyMT tumor progression (Calvo et al., 2013). Cdc42EP3 expression is already enhanced in hyperplasia-associated fibroblasts (HpAF) and maintained in adenoma-associated fibroblasts (AdAFs) and CAFs (Figures 7A and 7B). In agreement,

(C) Western blot showing the fibrillar (F) and soluble (G) content of actin, SEPT2, and SEPT7 in CAF#1 following control and Cdc42EP3 siRNA (siCEP3, smart pool). A 14-3-3 blot is also shown as a cytosolic control. See Figure S3D for quantification.

(D) Box and whisker plot showing the Young's elastic modulus of CAF#1 cells with control and Cdc42EP3 siRNA (siCEP3, smart pool). The central box represents the lower to upper quartiles; the middle line represents the mean. The horizontal line extends from the minimum to the maximum value ($n = 61$ single measurements for siCtr; $n = 53$ single measurements for siCEP3).

(E) Western blot showing the fibrillar (F) and soluble (G) content of actin, SEPT2, and SEPT7 in empty vector (−) and Flag-Cdc42EP3 (Flag-CEP3)-transfected NF#1. The histogram shows the F/G ratios of actin, SEPT2, and SEPT7. Bars represent mean ± SEM ($n = 3$).

(F) Top left inserts show GFP (green), SEPT2 (blue), and SEPT7 (red) staining of NF#1 following transfection with GFP or GFP-tagged Cdc42EP3 (CEP3) proteins. The grayscale panels show individual channel magnifications of perinuclear areas. Scale bars, 20 μm.

(G) Top left inserts show GFP (green) and actin (red) staining of NF#1 following transfection with GFP or GFP-tagged Cdc42EP3 (CEP3) proteins. The grayscale panels show individual channel magnifications of perinuclear areas. Scale bars, 20 μm.

(H) Histograms show fibrillar SEPT2&7 area (top) and F-actin stress fiber (SF) component (bottom) for the indicated experimental points. Bars represent mean ± SEM ($5 < n < 10$ single-cell measurements).

See also Figure S3.

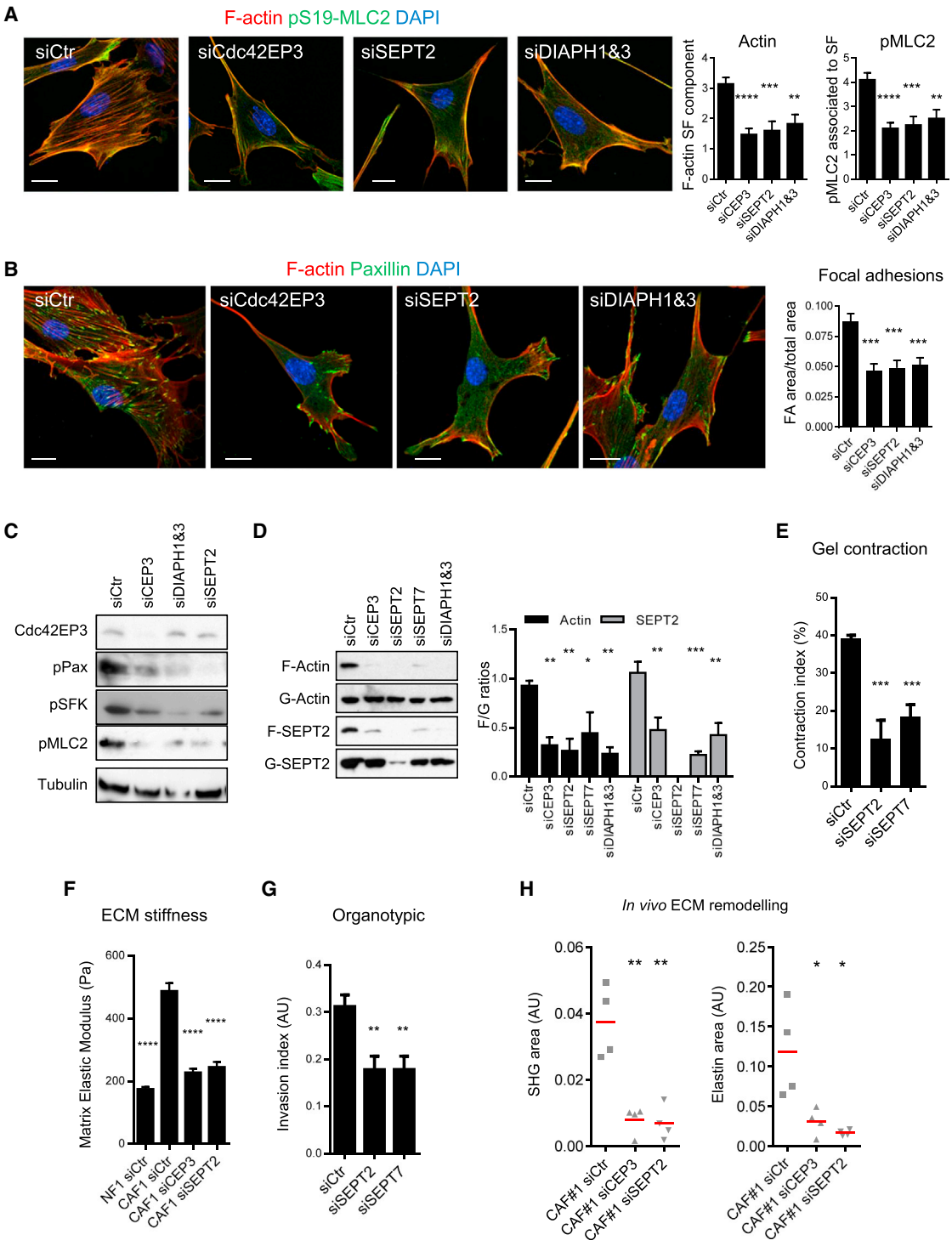

Figure 4. The Septin Cytoskeleton Is Required for CAF Functions

(A) Images showing F-actin (red), pS19-MLC2 (green), and DAPI (blue) staining of CAF#1 following control, Cdc42EP3, SEPT2, and DIAPH1&3 siRNA transfection (smart pools). Scale bars, 20 μm. Histograms show an F-actin stress fiber (SF) component and pMLC2 associated to SF for the indicated points. Bars represent mean ± SEM ($12 < n < 15$).

(B) Images show F-actin (red), paxillin (green), and DAPI (blue) staining of CAF#1 following with control, Cdc42EP3, SEPT2, and DIAPH1&3 siRNA transfection (smart pools). Scale bars, 20 μm. The histogram shows the focal adhesion (FA) area normalized to total cell area in single cells. Bars represent mean ± SEM ($10 < n < 12$).

(legend continued on next page)

increased levels of F-actin and insoluble filamentous septins were also evident in HpAFs and AdAFs (Figure 7C), as well as Src and paxillin phosphorylation (Figure 7D). Interestingly, Cdc42EP3 expression and cytoskeletal rearrangements preceded the strong activation of MLC2 in AdAFs and CAFs. Similarly, YAP activation, as determined by the expression of YAP target genes *Cyr61*, *Amotl2*, *Ankrd1*, and *Ctgf*, was only observed in AdAFs and CAFs (Figure 7E). These data indicate that increased Cdc42EP3 expression is an early event that precedes the highly contractile phenotype and activation of YAP in CAFs.

Many factors, including HGF, TGFβ, and SDF-1α, were able to induce *Cdc42ep3* mRNA in NFs. TGFβ and murine breast cancer cell (4T1) conditioned media (CM) yielded the greatest induction of Cdc42EP3 protein expression (Figures 7F and S7A). Consistently, treatment of NFs with either TGFβ or 4T1 CM for 48 hr triggered F-actin and septin rearrangements (Figures S7B and S7C), and phosphorylation of MLC2, Src-family kinases, and paxillin (Figure 7F). Furthermore, depletion of Cdc42EP3 prevented conditioned media from causing changes in the F/G ratios of actin and SEPT2, or in MLC2 and Src activation (Figures 7G and 7H). Gain-of-function experiments in NFs demonstrated that increasing the levels of Cdc42EP3 expression enhanced the ability of TGFβ and 4T1 CM to induce Src activation and elevated basal pS19-MLC2 levels (Figures S7D and S7E). These changes were associated with increased matrix remodeling after TGFβ- and 4T1 CM treatments (Figure S7F). Further, if contractility was boosted by overexpressing MLC2, as occurs in CAFs (Calvo et al., 2013), then a synergistic increase in matrix remodeling was observed in cells with high Cdc42EP3 levels (Figure S7G). These data suggest that elevated expression of Cdc42EP3 sensitizes cells to functional activation by the contractile cytoskeleton. We therefore tested whether elevated Cdc42EP3 levels were required for functional activation of NFs. Depletion of Cdc42EP3 prevented both the activation of collagen gel contraction and cancer cell invasion by NFs in response to cancer cell conditioned media (Figures 7I and 7J). Together, these data demonstrate that Cdc42EP3 is critical for the functional activation of normal fibroblasts by cancer cells.

DISCUSSION

Here, we describe Cdc42EP3 as a key regulator of the conversion of normal fibroblasts into CAFs. CAFs have enhanced stress fibers, αSMA-positive fibers, and focal adhesions (Calvo et al., 2013; Kalluri and Zeisberg, 2006; Öhlund et al., 2014; Sandbo et al., 2011; Xing et al., 2010). We now describe that CAFs are also characterized by increased levels of filamentous septins. These filaments are partly aligned with F-actin fibers in CAFs (Dolat et al., 2014; Joberty et al., 2001; Kinoshita et al., 1997). However, septin filaments and actin fibers do not precisely colocalize and time-lapse imaging indicated that the actin and septin networks exhibit different dynamic behaviors. During cytokinesis, the adaptor protein ANLN plays a key role in linking the actin and septin networks (Kinoshita et al., 2002), although recent work suggests that septins alone may be sufficient to drive formation of actin ring-like structures (Mavrakis et al., 2014). Our analyses indicate that Cdc42EP3 may play a similar role during interphase in CAFs. Cdc42EP3 can bind both actin and septins and localizes between F-actin fibers and SEPT2 filaments. Dynamic and mutational analysis suggests that Cdc42EP3 can bind to septins independent of binding to F-actin. We propose that dynamic septin filaments associated with Cdc42EP3 are then able to interact with actin filaments. Cdc42EP3 overexpression in NFs induces F-actin and septin polymerization, suggesting that connectivity between the two networks stabilizes them both. Indeed, the "cross brace" pattern of SEPT2 and Cdc42EP3 localization between stress fibers could provide mechanical support for the contractile actin cytoskeleton. This may allow for increased isometric tension in the F-actin network. These cytoskeletal changes are significant for both remodeling of the extracellular environment within tumors and cell signaling within CAFs, such as YAP activation. In the absence of Cdc42EP3, CAFs are unable to effectively remodel the ECM, leading to a reduction in matrix stiffness and less cancer cell invasion. In vivo analysis confirms the importance of Cdc42EP3 for ECM remodeling, as measured by collagen's second harmonic generation and elastin autofluorescence, and reveals that Cdc42EP3 is required for CAFs to promote angiogenesis. Similar loss-of-function phenotypes are observed when the septin network is depleted. Further, in vivo "admix" experiments with breast cancer cells demonstrate that Cdc42EP3 is required for efficient tumor growth. Our data establish that connectivity between the actin and septin networks is crucial for the function of CAFs from breast and squamous cell carcinoma. It will be interesting to determine the role of actin and septin networks in CAFs from pancreatic cancer, which can have both tumor-promoting and suppressive effects (Özdemir et al., 2014; Rhim et al., 2014).

Intriguingly, Cdc42EP3 upregulation precedes the emergence of highly contractile CAFs and YAP activation. Cdc42EP3 expression is already elevated in fibroblasts at the hyperplasia

(C) Western blot showing phosphorylated levels of pY118-paxillin (pPax), pY416-Src (pSFK), and pS19-MLC2 (pMLC2) in CAF#1 following transfection with control, Cdc42EP3 (CEP3), DIAPH1&3, and SEPT2 siRNA (smart pools). Cdc42EP3 and tubulin blots are also shown.
(D) Western blots showing fibrillar (F) and soluble (G) actin and SEPT2 in CAF#1 following control, Cdc42EP3 (CEP3), SEPT2, SEPT7, and DIAPH1&3 siRNA (smart pools). The histogram shows the F/G ratios of actin and SEPT2. Bars represent mean ± SEM (n = 5).
(E) Histogram shows gel contraction by CAF#1 following control, SEPT2, and SEPT7 siRNA (smart pools). Bars represent mean ± SEM (n = 8).
(F) Histogram shows the elastic modulus of matrices remodeled by NF#1 or CAF#1 following control, Cdc42EP3, or SEPT2 siRNA (smart pools). Bars indicate mean ± SD (n = 167 single measurements for NF-siCtr; n = 142 for CAF-siCtr; n = 173 for CAF-siCEP3; n = 51 for siSEPT2).
(G) Quantification of 4T1 invasion when co-cultured with CAF#1 transfected with control or SEPT2 and SEPT7 siRNA (smart pool). Bars represent mean ± SEM (n = 9 organotypic assays assessed over two experiments).
(H) Charts show second harmonic generation (SHG) of collagen fibers and elastin-positive areas in the CAF#1 matrix plugs transfected with control, Cdc42EP3 (CEP3), and SEPT2 siRNA. Line and error bars indicate mean ± SEM (n = 4 plugs from different mice).
See also Figure S4.

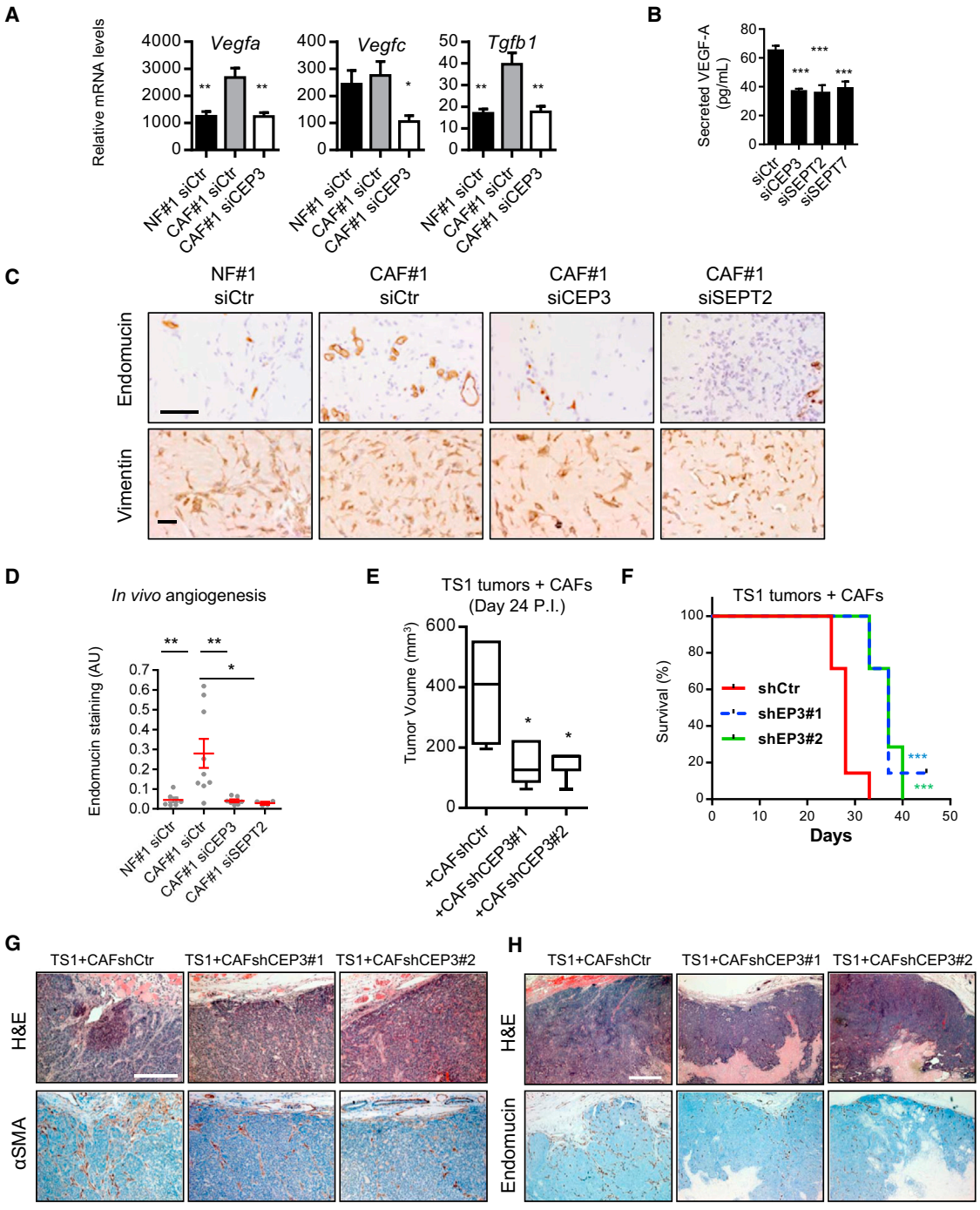

Figure 5. Cdc42EP3 Is Required for the Pro-tumorigenic Activity of CAFs In Vivo

(A) mRNA levels of angiogenic factors *Vegfa*, *Vegfc*, and *Tgfb1* in NF#1 and CAF#1 following transfection with control and Cdc42EP3 siRNA (CEP3, smart pool). Bars represent mean ± SEM (n = 12).

(B) Secreted levels of VEGF-A on CAF#1 following transfection with control, Cdc42EP3 (CEP3), SEPT2, or SEPT7 siRNA (smart pool). Bars represent mean ± SEM (n = 6).

(C) Representative images showing endomucin and vimentin staining of matrix plugs with NF#1 or CAF#1 transfected with control, Cdc42EP3 (CEP3), and SEPT2 siRNA (smart pools) and injected sub-cut in mice. Scale bars, 100 μm.

(D) Chart shows quantification of endomucin staining relative to fibroblast number (vimentin staining). Line and error bars indicate mean ± SEM (n = 7, except for CAF#1-siCtr that n = 9 and CAF#1-siSEPT2 that n = 5; each experimental point is an individual plug from a different mouse).

(legend continued on next page)

stage. Multiple signaling pathways converge upon *Cdc42EP3* promoter (Esnault et al., 2014; Gomis et al., 2006; McGee et al., 2011; Zhao et al., 2008). Therefore, Cdc42EP3 expression may be highly responsive to the small perturbations in tissue homeostasis that are likely to occur in hyperplastic tissue. However, this raises the question of why its expression does not lead to fully activated fibroblasts early in disease progression. It has been argued that both chemical and mechanical stimulation are needed for the acquisition of pathological active fibroblasts (Hinz, 2007). We propose that Cdc42EP3 is located at a node linking both activating processes. Soluble factors—either from hyperplastic epithelia or leukocytes infiltrating the pre-malignant tissue—could induce Cdc42EP3 expression in normal fibroblasts. This would sensitize the cells to mechanical cues, but in the absence of changes to the physical environment it would not trigger the activation of mechano-responsive signaling pathways. This is consistent with the small effect of Cdc42EP3 overexpression alone on NF function and the synergy observed when Cdc42EP3 and MLC2 are both overexpressed (Figure S7G). Further, when CAFs are grown on low stiffness gels (500 Pa, slightly above normal mouse mammary tissue stiffness) they do not form stress fibers or large focal adhesions and have only modest levels of nuclear YAP (Figures 6E–6G). Full activation of the highly contractile CAF phenotype and YAP activation would require concomitant stiffening of the ECM. The changes in the physical properties of the ECM are likely to happen with slow kinetics and may not coincide with the faster upregulation of Cdc42EP3 induced by soluble factors. This would explain why full pathological activation of fibroblasts does not occur early in disease progression (Calvo et al., 2013).

To conclude, we demonstrate a key role for coordination between the actin and the septin networks in CAFs. This is required for force-mediated matrix remodeling, promoting cancer cell invasion, angiogenesis, and tumor growth. Further, if coordination of F-actin and septin networks is prevented, then fibroblasts are unable to activate mechano-sensing signaling pathways, including paxillin phosphorylation, Src, and YAP. The elevated expression of Cdc42EP3 in the stroma of pre-malignant lesions enables the subsequent activation of these pathways and the emergence of fully activated CAFs.

EXPERIMENTAL PROCEDURES

cDNA, siRNA, and Reagents

Murine Cdc42EP3 cDNA was acquired from Thermo Scientific (pCMV-Sport 6-Cdc42EP3) and subcloned into pEGFP.C1 and PKR5.1-Flag. pEGFP-Cdc42EP3 was used to generate Cdc42EP3(IS-AA), Cdc42EP3(GPS-AAA), and Cdc42EP3(KLP-AAA) and was subcloned in pCSII-IRES to generate stable cells lines. pEGFP-MLC2 was a gift from Michael Olson (Beatson Institute). SEPT2-GFP and SEPT2-Cherry were a gift from Elias Spiliotis (Drexel University). MARS-Lifeact was a gift from Michael Sixt (Institute of Science and Technology). siRNA were purchased from Dharmacon and are listed in the Table S1. shRNA-targeting murine Cdc42EP3 were purchased from Thermo Scientific (pGIPZ backbone). The following growth factors and drugs were used: TGFβ (Peprotech), LPA (Sigma), HGF (Peprotech), and SDF-1 (Peprotech). Breast cancer cell conditioned medium was harvested from 4T1 cells in DMEM 1% fetal bovine serum (FBS) for 48 hr and filtered through a 0.22-μm filter. Fibroblasts were transfected with 100 nM siRNA using DharmaFECT 1 (Dharmacon) and Lipofectamine (Life Technologies) for plasmids.

Cell Lines

Fibroblasts from normal mammary glands (NFs), hyperplastic mammary tissue (HpAFs), mammary adenoma/early carcinoma tissue (AdAFs), and mammary carcinoma (CAFs) have been previously described (Calvo et al., 2013). Fibroblasts were cultured in DMEM (Invitrogen), 10% FBS, and 1% insulin-selenium-transferrin (ITS). 4T1 murine breast cancer cells were used for the organotypic invasion assays and to generate breast cancer cell conditioned media. SCC12 human squamous cell carcinoma cells were used for organotypic invasion assays of HN-CAF and Cer-CAF. MMTV-PyMT TS1 murine breast cancer cells were used to generate orthotopic tumors in syngeneic FVB/n mice. Cell lines stably expressing Cdc42EP3-GFP, shRNA control, and shRNA-targeting murine Cdc42EP3 were generated by lentiviral infection. NF#1 stably expressing Cdc42EP3-GFP were sorted into low (NF#1-Cdc42EP3-GFP^{low}) and high (NF#1-Cdc42EP3-GFP^{high}) expression by fluorescence-activated cell sorting.

ECM Remodeling and Invasion Assays

ECM-remodeling (contraction) assays and human SCC CAF and mouse mammary CAFs organotypic culture systems were as previously described (Calvo et al., 2013). Details are provided in the Supplemental Experimental Procedures.

Screening

Smart-pool siRNA were transiently transfected into two individual CAF lines (CAF#1 and CAF#2). The functional role of each gene was assessed using collagen gel contraction assays and 4T1 breast cancer cell organotypic invasion assays. Each experimental point was normalized against the control siRNA for that experiment.

Biophysical Methods

AFM was performed as described (Calvo et al., 2013), and details are provided in the Supplemental Experimental Procedures. Polyacrylamide gels of defined elastic moduli were made as described (Yeung et al., 2005).

Immunofluorescence

Cells were fixed in 4% paraformaldehyde, except for the analysis of endogenous septins when cells were fixed in ice-cold methanol for 10 min. Cells were permeabilized by incubation in PBS 0.5% NP-40 (Sigma) at 4°C for 20 min (twice), PBS 0.3% Triton 100 (Sigma) at room temperature (RT) for 20 min, and PBS 0.1% Triton 100 at room temperature (RT) for 15 min (twice). Samples were blocked in 4% BSA PBS 0.05% Tween20 (Sigma) and

(E) Box and whisker plot showing volumes of orthotopic tumors generated by co-injection of TS1 murine MMTV-PyMT breast cancer cells with CAF#3 stably expressing control or two different shRNA targeting Cdc42EP3. The central box represents the lower to upper quartiles; the middle line represents the mean; and the horizontal line extends from the minimum to the maximum value (n = 7, except for CAF-shCtr that n = 6). Tumors were measured at day 24 post-injection.
(F) Survival curves for orthotopic tumors generated by co-injection of TS1 murine MMTV-PyMT breast cancer cells with CAF#3 stably expressing control or two different shRNA targeting Cdc42EP3. The survival curve represents the percentage of animals alive at the indicated time point after injection. Survival curves were estimated by the Kaplan-Meier method and compared among subsets using the log rank test.
(G) Representative images of orthotopic tumors generated by co-injection of TS1 murine MMTV-PyMT breast cancer cells with CAF#3 stably expressing control or two different shRNA targeting Cdc42EP3 and stained for H&E or αSMA. Scale bar, 500 μm.
(H) Representative images of orthotopic tumors generated by co-injection of TS1 murine MMTV-PyMT breast cancer cells with CAF#3 stably expressing control or two different shRNA targeting Cdc42EP3 and stained for H&E or endomucin. Scale bar, 200 μm.
See also Figure S5.

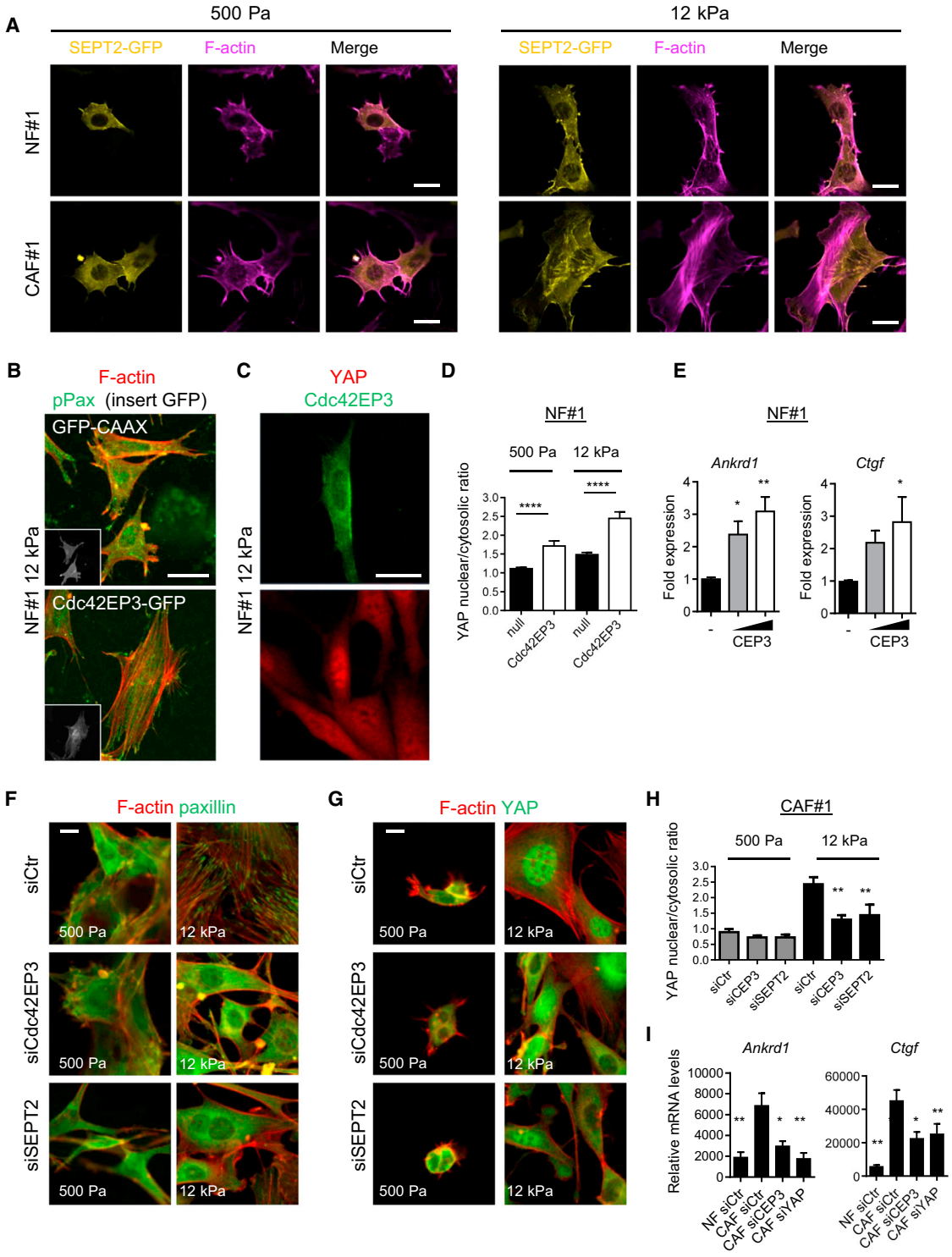

Figure 6. Cdc42EP3 Is Required for Mechano-sensing

(A) Images show single and merged channels of SEPT2-GFP (yellow) and F-actin (magenta) staining of NF#1 and CAF#1 when seeded on soft (~500 Pa) and stiff (~12 kPa) matrices. Scale bar represents 10 μm.

(B) Images show F-actin (red) and pY118-Paxillin (pPax) staining of NF#1 when seeded on stiff (~12 kPa) matrices following transfection with GFP-CAAX and Cdc42EP3-GFP. Inserts show GFP signal (grayscale). Scale bar represents 10 μm.

(legend continued on next page)

incubated with primary antibody in blocking solution overnight at 4°C. After three PBS washes, secondary antibody in blocking solution was added for 3 hr. After three PBS washes, samples were mounted and analyzed using an inverted Zeiss LSM780/Leica SP8. For analysis of fibronectin production, cells were kept in 1% FBS for 24 hr before fixing and were permeabilized for only 5 min in 0.1% Triton 100 at RT during the staining procedure to reduce detection of intracellular protein. Antibody description and working dilutions can be found in Table S2. Time-lapse microscopy was performed using a Zeiss LSM780 with cells in CO_2-independent media (GIBCO) containing 10% FBS. The details of the imaging analysis methods are provided in the Supplemental Experimental Procedures.

Structured Illumination Microscopy

Cells were processed for immunostaining as usual and mounted in a 1:1 mixture of glycerol and MOWIOL. Imaging was performed using a Zeiss ELYRA PS1 and data processed using the SIM tools in the Zen 2011 software. Channel alignment was performed with 0.1-μm TetraSpeck fluorescent microspheres (Life Technologies).

Collagenase Activity Measurements

A thin layer of collagen gel (4.6 mg/ml) containing 50 μg/ml of ^{DQ}FITC-Collagen I from bovine skin (Life Technologies) and 10% FBS was generated. After 1 hr, fibroblasts were seeded on top. After 48 hr, samples were fixed in 4% paraformaldehyde for 1 hr and stained for F-actin. A fluorescein isothiocyanate signal generated by cleaved collagen and F-actin staining was detected using an inverted Leica SP8 microscope.

F-G Actin and Septin Fractionation

We determined the relative proportions of filamentous and globular actin and septins by sedimentation, followed by quantitative analysis by SDS-PAGE. Cells were lysed in warm F-actin stabilization buffer (PIPES 100 mM [pH 6.9], 5 mM $MgCl_2$, 1 mM EGTA, 30% glycerol, 0.1% Triton X-100, 0.1% NP-40, 0.1% Tween-20, 0.15% 2-mercaptoethanol, 1 mM ATP, and complete EDTA-free cocktail) and homogenized using a 25G gauge. Lysates were incubated for 10 min at 37°C, and cellular debris was removed by centrifugation at room temperature. Supernatants were then subjected to ultracentrifugation at 37°C (1 hr at 100,000 *g*). Supernatants containing the globular cytosolic fraction (G fraction) were removed. Using a similar volume of 10 mM $CaCl_2$ 10 μM Cytochalasin D, the pellet containing the fibrillar fraction (F fraction) was dissolved for 1 hr in ice. Both G and F fractions were mixed with 5× sample buffer before western blot analysis. Antibody description and working dilutions can be found in Table S2.

In Vitro F-actin Binding Assay

Human platelet actin (Cytoskeleton, Actin Binding Protein Biochem Kit #BK013) in general actin buffer (5 mM Tris-HCl [pH 8.0] and 0.2 mM $CaCl_2$, supplemented with 0.2 mM ATP) was polymerized using actin polymerization buffer (50 mM KCl, 2 mM $MgCl_2$, and 1 mM ATP) at 24°C for 1 hr. 0.3 μM GST-Cdc42EP3 (Abcam, ab161060) and recombinant 0.3 μM glutathione S-transferase (GST) (Sigma-Aldrich; SRP5348) were incubated with 20 μM F-actin for 1 hr at 24°C and centrifuged at 150,000 *g* for 90 min at 24°C. Equal volumes of the supernatant and pellet fractions were resolved using a 4%–12% SDS-PAGE gel, stained with InstantBlue (Expedeon) for actin staining, and further processed by western blotting (for GST and GST-Cdc42EP3) analysis.

Immunoprecipitation

GFP-Cdc42EP3 immunoprecipitations were performed in HEK293 cells. Cells were transiently transfected and subsequently lysed in NP-40 lysis buffer (50 mM Tris [pH 7.4], 150 mM NaCl, 1 mM EDTA, and 1% NP-40). Lysates were cleared by centrifugation and supernatants were further cleared by pre-incubating with 25 μl of G-sepharose. Cleared supernatants were then mixed with 2 μg of anti-GFP antibody plus 25 μl of G-sepharose and incubated for 2 hr at 4°C. Immunoprecipitations were then washed four times with NP-40 washing buffer (50 mM Tris [pH 7.4], 150 mM NaCl, 1 mM EDTA, 1% NP40, and 0.25% gelatin) before adding sample buffer. Antibody details can be found in Table S2.

Western Blotting

Unless stated otherwise, all protein lysates were obtained from cells seeded on top of a thin layer of a mixture of collagen I:Matrigel matrices. Western blot exposures within the dynamic range were obtained on film and quantified by densitometry with the program NIH Image 1.60, except for Figures S1B, S3I, and S7D, which were generated with the Azure c300 scanner. Antibody details can be found in Table S2.

Detection of VEGF-A in Conditioned Media

ELISA was used to assess the levels of secreted murine VEGF-A in accordance with the manufacturers' instructions (R&D; Mouse VEGF DY493-05). 10^5 cells were seeded on 12-well plates, and 24 hr later cells were washed and 0.6 ml of DMEM supplemented with 0.5% FBS added to each well. Medium was collected and assayed after 24 hr of conditioning.

In Vivo Matrigel Plugs

2×10^6 fibroblasts were suspended in 100 μl of PBS and mixed in 300 μl of Matrigel. Then 300 μl of the mixture were injected subcutaneously on the mammary fat pad of a 12-week-old FVB/n female. After 7 days, the plugs were fixed in 4% paraformaldehyde. Blood vessel density was calculated by normalizing the area of endomucin staining to the area of vimentin staining of all the slices processed. Antibody details are in Table S2. Collagen second harmonic generation (SHG) and elastin signal were acquired by excitation of sections with an 880-nm pulsed Ti-Sapphire laser and emitted light acquired at 440 nm (SHG) and 535 nm (Elastin) using a Leica SP8 microscope.

Generation of Syngeneic Orthotopic Tumors

MMTV-PyMT TS1 murine breast cancer cells were used to generate orthotopic tumors in wild-type FBV/n mice. 10^6 TS1 cells and 3×10^6 CAFs (shRNA control, shRNA-Cdc42EP3#1, or shRNA-Cdc42EP3#2) were suspended in 100 μl

(C) Images show GFP (green) and YAP (red) staining of NF#1 when seeded stiff (~12 kPa) matrices following transfection with Cdc42EP3-GFP. Scale bar represents 10 μm.

(D) Histogram shows nuclear YAP fluorescent intensity/cytoplasmic YAP fluorescent intensity of NF#1 when seeded on soft (~500 Pa) and stiff (~12 kPa) matrices following transfection with GFP-CAAX or Cdc42EP3-GFP. The mean and 95% confidence interval are shown ($23 < n < 80$ cells).

(E) Fold mRNA levels of YAP target genes *Ankrd1* and *Ctgf* in stable cell lines NF#1 null, NF#1-Cdc42EP3^{low}, and NF#1-Cdc42EP3^{high} maintained in 1% FBS for 6 hr. Bars represent mean ± SEM ($n = 5$).

(F) Images show F-actin (red) and paxillin (green) staining of CAF#1 when seeded on soft (~500 Pa) and stiff (~12 kPa) matrices following transfection with control, Cdc42EP3, or SEPT2 siRNA (smart pools). Scale bar represents 10 μm.

(G) Images show F-actin (red) and YAP (green) staining of CAF#1 when seeded on soft (~500 Pa) and stiff (~12 kPa) matrices following transfection with control, Cdc42EP3, or SEPT2 siRNA (smart pools). Scale bar is 10 μm.

(H) Histogram shows nuclear YAP fluorescent intensity/cytoplasmic YAP fluorescent intensity for the indicated conditions. The mean and 95% confidence interval are shown ($23 < n < 80$ cells).

(I) Relative mRNA levels of YAP target genes *Ankrd1* and *Ctgf* in NF#1 and CAF#1 following transfection with control, Cdc42EP3 (CEP3), and YAP siRNA (smart pools). Bars represent mean ± SEM ($n = 6$).

See also Figure S6.

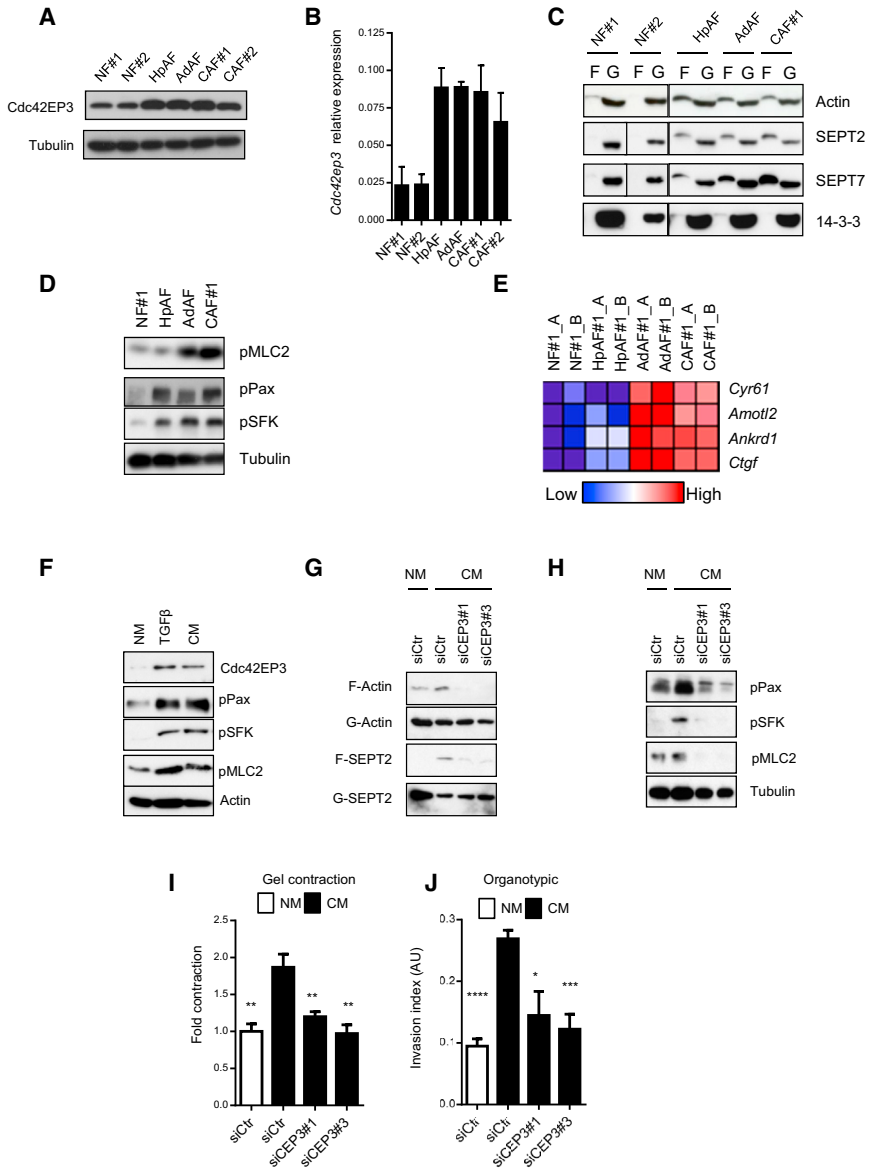

Figure 7. Cdc42EP3 Is Induced and Required Early in Fibroblast Activation

(A) Western blots of Cdc42EP3 in fibroblasts isolated from different disease stages (NF, HpAF, AdAF, and CAF).

(B) Relative levels of *Cdc42ep3* mRNA in fibroblasts from different disease stages. Bars indicate mean ± SEM (n = 4).

(C) Western blot showing the fibrillar (F) and soluble (G) actin, SEPT2, and SEPT7 in fibroblasts from different disease stages. A 14-3-3 blot is also shown as an internal cytosolic control.

(D) Western blots showing pY118-paxillin (pPax), pY416-Src (pSFK), and pS19-MLC2 (pMLC2) and tubulin levels in fibroblasts isolated from different disease stages.

(E) GSEA-derived heatmap showing the relative levels of mRNA expression of YAP target genes (*Cyr61*, *Amotl2*, *Ankrd1*, and *Ctgf*) in fibroblasts isolated from different disease stages on duplicate. Colors range from dark red to dark blue, representing, respectively, the highest and lowest normalized expression of the gene.

(F) Western blots showing pY118-paxillin (pPax), pY416-Src (pSFK), and pS19-MLC2 (pMLC2) in NF#1 subjected to 1% FBS (NM), TGFβ (2 ng/ml), and breast cancer cell conditioned media (CM) for 48 hr. Cdc42EP3 and actin blots are also shown.

(G) Western blots of fibrillar (F) and soluble (G) fractions of actin and SEPT2 in NF#1 subjected to 1% FBS (NM) or breast cancer cell conditioned media (CM) following transfection with control and two single Cdc42EP3 (CEP3) siRNA.

(H) Western blots showing tubulin and pY118-paxillin (pPax), pY416-Src (pSFK), and pS19-MLC2 (pMLC2) in NF#1 subjected to 1% FBS (NM) or breast cancer cell conditioned media (CM) following transfection with control and two single Cdc42EP3 (CEP3) siRNA.

(I) Histogram showing gel contraction of NF#1 subjected to normal media (NM) or breast cancer cell conditioned media (CM) following transfection with control and two single Cdc42EP3 (CEP3) siRNA. Bars represent mean ± SEM (n = 5).

(J) Histogram showing organotypic cancer cell invasion of NF#1 subjected to normal media (NM) or breast cancer cell conditioned media (CM) following transfection with control two single Cdc42EP3 (CEP3) siRNA. Bars represent mean ± SEM (n = 5). See also Figure S7.

of PBS:Matrigel (50:50) and injected orthotopically into the mammary fat pad of 6- to 8-week-old females. To calculate tumor volume, the formula V = (length × width^2)/2 was used. Tumors were fixed in 4% paraformaldehyde for histological analysis. Antibody description and working dilutions can be found in Table S2. Mice were kept in accordance with UK regulations under project license PPL 70/ 8380.

mRNA Analysis

RNA was isolated using an RNeasy Kit (QIAGEN). Reverse transcription was performed using Precision nanoScript 2 Reverse-Transcription Kit (PrimerDesign), and qPCR was performed using PrecisionPLUS 2x qPCR MasterMix with ROX and SybrGreen (PrimerDesign). Oligonucleotides for qRT-PCR are described in the Table S3. Expression levels are normalized to the expression of *Gapdh*, *Rplp1*, or *Lamc2*. Gene-set enrichment analyses (GSEA) details are provided in the Supplemental Experimental Procedures.

Analysis of Expression in Clinical Samples

mRNA levels of BORG family members in the stromal compartment of human tumors were obtained from GSE9014 (Finak breast dataset) and GSE8977 (Karnoub breast dataset) (Finak et al., 2008; Karnoub et al., 2007). Probes on the Finak dataset were A_23_P166453 (CDC42EP1), A_23_P1602 (CDC42EP2), A_23_P209636 (CDC42EP3), A_23_P66891 (CDC42EP4), and A_24_P44916 (CDC42EP5). Probes on the Karnoub dataset were 204693_at (CDC42EP1), 214014_at (CDC42EP2), 225685_at (CDC42EP3), 218062_x_at (CDC42EP4), and 227850_x_at (CDC42EP5).

Statistical Analyses

Paired or unpaired two-tailed Student's t test, Mann-Whitney's test, and one-way ANOVA with Tukey post-test (for multiple comparisons) were performed using GraphPad Prism (GraphPad Software). Unless stated otherwise, mean values and SEM are shown. Survival curves were estimated based on the

Kaplan-Meier method and compared using a log rank test. p values of less than 0.05 are considered statistically significant: *, $p < 0.05$; **, $p < 0.01$; ***, $p < 0.001$; ****, $p < 0.0001$; ns, non-significant.

SUPPLEMENTAL INFORMATION

Supplemental Information includes Supplemental Experimental Procedures, seven figures, three tables, and four movies and can be found with this article online at http://dx.doi.org/10.1016/j.celrep.2015.11.052.

AUTHOR CONTRIBUTIONS

F.C. and E.S. carried out all of the experiments (except those noted otherwise), conceived of the study, and wrote the manuscript. R.R. assisted in qPCR, western blotting, ELISA, in vitro F-actin binding assays, and F-G analyses. S.H. assisted with in vivo experiments. A.J.F. assisted in cloning and the generation of stable cell lines. E.M. and G.C. performed all of the AFM analyses. A.B. and F.B. contributed to the SIM experiments. All authors critically read the manuscript and provided intellectual input.

ACKNOWLEDGMENTS

F.C. was funded by Cancer Research UK, the Institute of Cancer Research, and Worldwide Cancer Research (grant 15-0273). E.S. was funded by Cancer Research UK (grant CRUK_A5317). A.B., F.B. and E.S. were funded by Cancer Research UK and the Francis Crick Institute (grant number FCI01), which receives its core funding from Cancer Research UK, the UK Medical Research Council, and the Wellcome Trust. G.C. is in receipt of a Royal Society University Research Fellowship. We thank Drs. Spiliotis, Sixt, and Olson for plasmids and lab members for help and advice. Finally, we would like to dedicate this work to the memory of Chris Marshall. He was an amazing colleague whose scientific brilliance and humanity will continue to inspire us.

Received: February 17, 2015
Revised: September 11, 2015
Accepted: November 16, 2015
Published: December 17, 2015

REFERENCES

Bahou, W.F., Campbell, A.D., and Wicha, M.S. (1992). cDNA cloning and molecular characterization of MSE55, a novel human serum constituent protein that displays bone marrow stromal/endothelial cell-specific expression. J. Biol. Chem. *267*, 13986–13992.

Bhowmick, N.A., and Moses, H.L. (2005). Tumor-stroma interactions. Curr. Opin. Genet. Dev. *15*, 97–101.

Calvo, F., and Sahai, E. (2011). Cell communication networks in cancer invasion. Curr. Opin. Cell Biol. *23*, 621–629.

Calvo, F., Ege, N., Grande-Garcia, A., Hooper, S., Jenkins, R.P., Chaudhry, S.I., Harrington, K., Williamson, P., Moeendarbary, E., Charras, G., and Sahai, E. (2013). Mechanotransduction and YAP-dependent matrix remodelling is required for the generation and maintenance of cancer-associated fibroblasts. Nat. Cell Biol. *15*, 637–646.

Deakin, N.O., and Turner, C.E. (2008). Paxillin comes of age. J. Cell Sci. *121*, 2435–2444.

Dolat, L., Hunyara, J.L., Bowen, J.R., Karasmanis, E.P., Elgawly, M., Galkin, V.E., and Spiliotis, E.T. (2014). Septins promote stress fiber-mediated maturation of focal adhesions and renal epithelial motility. J. Cell Biol. *207*, 225–235.

DuFort, C.C., Paszek, M.J., and Weaver, V.M. (2011). Balancing forces: architectural control of mechanotransduction. Nat. Rev. Mol. Cell Biol. *12*, 308–319.

Dupont, S., Morsut, L., Aragona, M., Enzo, E., Giulitti, S., Cordenonsi, M., Zanconato, F., Le Digabel, J., Forcato, M., Bicciato, S., et al. (2011). Role of YAP/TAZ in mechanotransduction. Nature *474*, 179–183.

Esnault, C., Stewart, A., Gualdrini, F., East, P., Horswell, S., Matthews, N., and Treisman, R. (2014). Rho-actin signaling to the MRTF coactivators dominates the immediate transcriptional response to serum in fibroblasts. Genes Dev. *28*, 943–958.

Field, C.M., and Alberts, B.M. (1995). Anillin, a contractile ring protein that cycles from the nucleus to the cell cortex. J. Cell Biol. *131*, 165–178.

Finak, G., Bertos, N., Pepin, F., Sadekova, S., Souleimanova, M., Zhao, H., Chen, H., Omeroglu, G., Meterissian, S., Omeroglu, A., et al. (2008). Stromal gene expression predicts clinical outcome in breast cancer. Nat. Med. *14*, 518–527.

Friederich, E., Vancompernolle, K., Huet, C., Goethals, M., Finidori, J., Vandekerckhove, J., and Louvard, D. (1992). An actin-binding site containing a conserved motif of charged amino acid residues is essential for the morphogenic effect of villin. Cell *70*, 81–92.

Gaggioli, C., Hooper, S., Hidalgo-Carcedo, C., Grosse, R., Marshall, J.F., Harrington, K., and Sahai, E. (2007). Fibroblast-led collective invasion of carcinoma cells with differing roles for RhoGTPases in leading and following cells. Nat. Cell Biol. *9*, 1392–1400.

Gomis, R.R., Alarcón, C., He, W., Wang, Q., Seoane, J., Lash, A., and Massagué, J. (2006). A FoxO-Smad synexpression group in human keratinocytes. Proc. Natl. Acad. Sci. USA *103*, 12747–12752.

Hanahan, D., and Coussens, L.M. (2012). Accessories to the crime: functions of cells recruited to the tumor microenvironment. Cancer Cell *21*, 309–322.

Hinz, B. (2007). Formation and function of the myofibroblast during tissue repair. J. Invest. Dermatol. *127*, 526–537.

Hirsch, D.S., Pirone, D.M., and Burbelo, P.D. (2001). A new family of Cdc42 effector proteins, CEPs, function in fibroblast and epithelial cell shape changes. J. Biol. Chem. *276*, 875–883.

Joberty, G., Perlungher, R.R., and Macara, I.G. (1999). The Borgs, a new family of Cdc42 and TC10 GTPase-interacting proteins. Mol. Cell. Biol. *19*, 6585–6597.

Joberty, G., Perlungher, R.R., Sheffield, P.J., Kinoshita, M., Noda, M., Haystead, T., and Macara, I.G. (2001). Borg proteins control septin organization and are negatively regulated by Cdc42. Nat. Cell Biol. *3*, 861–866.

Joyce, J.A., and Pollard, J.W. (2009). Microenvironmental regulation of metastasis. Nat. Rev. Cancer *9*, 239–252.

Kalluri, R., and Zeisberg, M. (2006). Fibroblasts in cancer. Nat. Rev. Cancer *6*, 392–401.

Karnoub, A.E., Dash, A.B., Vo, A.P., Sullivan, A., Brooks, M.W., Bell, G.W., Richardson, A.L., Polyak, K., Tubo, R., and Weinberg, R.A. (2007). Mesenchymal stem cells within tumour stroma promote breast cancer metastasis. Nature *449*, 557–563.

Kinoshita, M., Kumar, S., Mizoguchi, A., Ide, C., Kinoshita, A., Haraguchi, T., Hiraoka, Y., and Noda, M. (1997). Nedd5, a mammalian septin, is a novel cytoskeletal component interacting with actin-based structures. Genes Dev. *11*, 1535–1547.

Kinoshita, M., Field, C.M., Coughlin, M.L., Straight, A.F., and Mitchison, T.J. (2002). Self- and actin-templated assembly of Mammalian septins. Dev. Cell *3*, 791–802.

Levental, K.R., Yu, H., Kass, L., Lakins, J.N., Egeblad, M., Erler, J.T., Fong, S.F., Csiszar, K., Giaccia, A., Weninger, W., et al. (2009). Matrix crosslinking forces tumor progression by enhancing integrin signaling. Cell *139*, 891–906.

Mavrakis, M., Azou-Gros, Y., Tsai, F.C., Alvarado, J., Bertin, A., Iv, F., Kress, A., Brasselet, S., Koenderink, G.H., and Lecuit, T. (2014). Septins promote F-actin ring formation by crosslinking actin filaments into curved bundles. Nat. Cell Biol. *16*, 322–334.

McGee, K.M., Vartiainen, M.K., Khaw, P.T., Treisman, R., and Bailly, M. (2011). Nuclear transport of the serum response factor coactivator MRTF-A is downregulated at tensional homeostasis. EMBO Rep. *12*, 963–970.

Mostowy, S., and Cossart, P. (2012). Septins: the fourth component of the cytoskeleton. Nat. Rev. Mol. Cell Biol. *13*, 183–194.

Narumiya, S., Tanji, M., and Ishizaki, T. (2009). Rho signaling, ROCK and mDia1, in transformation, metastasis and invasion. Cancer Metastasis Rev. *28*, 65–76.

Öhlund, D., Elyada, E., and Tuveson, D. (2014). Fibroblast heterogeneity in the cancer wound. J. Exp. Med. *211*, 1503–1523.

Özdemir, B.C., Pentcheva-Hoang, T., Carstens, J.L., Zheng, X., Wu, C.C., Simpson, T.R., Laklai, H., Sugimoto, H., Kahlert, C., Novitskiy, S.V., et al. (2014). Depletion of carcinoma-associated fibroblasts and fibrosis induces immunosuppression and accelerates pancreas cancer with reduced survival. Cancer Cell *25*, 719–734.

Paszek, M.J., Zahir, N., Johnson, K.R., Lakins, J.N., Rozenberg, G.I., Gefen, A., Reinhart-King, C.A., Margulies, S.S., Dembo, M., Boettiger, D., et al. (2005). Tensional homeostasis and the malignant phenotype. Cancer Cell *8*, 241–254.

Posern, G., Sotiropoulos, A., and Treisman, R. (2002). Mutant actins demonstrate a role for unpolymerized actin in control of transcription by serum response factor. Mol. Biol. Cell *13*, 4167–4178.

Rhim, A.D., Oberstein, P.E., Thomas, D.H., Mirek, E.T., Palermo, C.F., Sastra, S.A., Dekleva, E.N., Saunders, T., Becerra, C.P., Tattersall, I.W., et al. (2014). Stromal elements act to restrain, rather than support, pancreatic ductal adenocarcinoma. Cancer Cell *25*, 735–747.

Sandbo, N., Ngam, C., Yau, D., Kach, J., and Dulin, N.O. (2011). Delayed transcriptional regulation by actin dynamics/MKL-1 during myofibroblast differentiation in human lung fibroblasts. Am. J. Resp. Crit. Care *183*, A3568–A3568.

Sheffield, P.J., Oliver, C.J., Kremer, B.E., Sheng, S., Shao, Z., and Macara, I.G. (2003). Borg/septin interactions and the assembly of mammalian septin heterodimers, trimers, and filaments. J. Biol. Chem. *278*, 3483–3488.

Sirajuddin, M., Farkasovsky, M., Hauer, F., Kühlmann, D., Macara, I.G., Weyand, M., Stark, H., and Wittinghofer, A. (2007). Structural insight into filament formation by mammalian septins. Nature *449*, 311–315.

Weirich, C.S., Erzberger, J.P., and Barral, Y. (2008). The septin family of GTPases: architecture and dynamics. Nat. Rev. Mol. Cell Biol. *9*, 478–489.

Xing, F., Saidou, J., and Watabe, K. (2010). Cancer associated fibroblasts (CAFs) in tumor microenvironment. Front. Biosci. (Landmark Ed.) *15*, 166–179.

Yeung, T., Georges, P.C., Flanagan, L.A., Marg, B., Ortiz, M., Funaki, M., Zahir, N., Ming, W., Weaver, V., and Janmey, P.A. (2005). Effects of substrate stiffness on cell morphology, cytoskeletal structure, and adhesion. Cell Motil. Cytoskeleton *60*, 24–34.

Zhao, B., Ye, X., Yu, J., Li, L., Li, W., Li, S., Yu, J., Lin, J.D., Wang, C.Y., Chinnaiyan, A.M., et al. (2008). TEAD mediates YAP-dependent gene induction and growth control. Genes Dev. *22*, 1962–1971.

Cell Reports

Supplemental Information

Cdc42EP3/BORG2 and Septin Network Enables Mechano-transduction and the Emergence of Cancer-Associated Fibroblasts

Fernando Calvo, Romana Ranftl, Steven Hooper, Aaron J. Farrugia, Emad Moeendarbary, Andreas Bruckbauer, Facundo Batista, Guillaume Charras, and Erik Sahai

Inventory of Supplemental Information for

"Cdc42EP3/BORG2 and septin network enables mechano-transduction and the emergence of cancer-associated fibroblasts"

Correspondence to:

- Dr Fernando Calvo, Tumour Microenvironment Team, Division of Cancer Biology, Institute of Cancer Research, 237 Fulham Road, London, SW2 6JB, UK. Phone: +44 (0) 207 153 5129; fernando.calvo@icr.ac.uk.

- Dr Erik Sahai, Tumour Cell Biology Laboratory, Francis Crick Institute, 44 Lincoln's Inn Fields, London, WC2A 3LY, UK. Phone: +44 (0) 207 269 3125; erik.sahai@crick.ac.uk.

- **Supplemental Experimental Procedures**
- **Supplemental Figures S1-S7**
- **Supplemental Tables S1-S3**
- **Supplemental Movie S1, related to Figure 2**. CAF expressing MARS-Lifeact (red) and SEPT2-GFP (green) was imaged every 10 seconds.
- **Supplemental Movie S2, related to Figure 2**. NF expressing MARS-Lifeact (red) and SEPT2-GFP (green) was imaged every 10 seconds.
- **Supplemental Movie S3, related to Figure 2**. CAF expressing MARS-Lifeact (red) and CDC42EP3-GFP (green) was imaged every 10 seconds.
- **Supplemental Movie S4, related to Figure 2**. CAF expressing SEPT2-Cherry (red) and CDC42EP3-GFP (green) was imaged every 10 seconds.

Supplemental Experimental Procedures

ECM-remodeling assays

To assess force-mediated matrix remodeling, 75 × 10^3 fibroblasts were embedded in 100 µL of a mixture of Collagen I (BD Biosciences) and Matrigel (BD Biosciences) yielding a final collagen concentration of ~4.6 mg/mL and a final Matrigel concentration of ~2.2 mg/mL (Collagen I:Matrigel matrix hereafter) and seeded on a 35 mm glass bottom MatTek dish (MatTek Co.). Once the gel was set, cells were maintained in DMEM + 10% FBS (unless otherwise stated) + 1% ITS. Unless stated otherwise, the gel contraction value refers to the contraction observed after 3 days. To obtain the gel contraction value, the relative diameter of the well and the gel were measured using ImageJ software, and the percentage of contraction was calculated using the formula 100 × (well diameter – gel diameter) / well diameter.

Invasion assays

The invasion index was calculated by measuring the total area over which breast cancer cells had dispersed (including invading and non-invading cells) and the area of non-invading cells. The value shown is the average of the measurement (1 – [non-invading area/total area]) of at least ten measurements from two or more independent experiments and the error bars represent the SEM. MATLAB script was used to automatically identify the total cell area and the non-invading area. The M files are available on request, email robert.jenkins@crick.ac.uk

Atomic Force Microscopy (AFM)

In brief, to assess the elastic modulus of gels remodeled by fibroblasts, 75 × 10^3 fibroblasts were embedded in 100 µL of Collagen I:Matrigel and seeded on ultra-low attachment 96 well plate well (Costar). Once the gels were set, they were maintained in DMEM + 10% FCS + 1% ITS. After 3 days, the elastic modulus of the gels was measured. On the day of the experiment, the gels were gently lifted from their well and fixed in the center of 50 mm glass bottom petri dishes (Fluorodish) using cyanoacrylate superglue. After 5 min, Leibovitz L-15 medium (Invitrogen) supplemented with 10% FCS was added to the dish. To assess the elastic modulus of the different fibroblasts, 75 × 10^3 cells were seeded into 50 mm glass bottom petri dishes in DMEM + 10% FCS + 1% ITS. After 2 days, their elastic modulus was measured. AFM measurements were

performed using a JPK Nanowizard-I (JPK instruments) interfaced to an inverted optical microscope (IX-81, Olympus). AFM cantilevers with pyramidal tips (MLCT) and nominal spring constants of 0.07 Nm^{-1} were modified by gluing beads to the cantilever underside with UV curing glue. 35 μm radius glass beads and 7.5 μm radius latex beads (Invitrogen) were used for indentation experiments on gels and cells respectively. Cantilever spring constants were determined prior to modification using the thermal noise method implemented in the AFM software (JPK SPM). Prior to any indentation tests, the sensitivity of the cantilever was set by measuring the slope of force-distance curves acquired on glass regions of the petri dish. For indentation experiments on gels the optical microscope was used to align the tip of the cantilever over regions in the middle of the gel and, for each gel, measurements were acquired in 30-40 locations ~100 μm apart. For AFM measurements on cells the tip of the cantilever was aligned over regions on top of the cell nucleus and measurements were acquired in two locations a few microns apart. Force-distance curves were acquired with an approach speed of 5 $\mu m.s^{-1}$ until reaching the maximum set force of 3 nN and 2 nN for gels and cells, respectively. After the experiment, the elastic moduli were extracted from the force-distance curves by fitting the contact portion of curves to a Hertz contact model. For each force-distance curve, goodness of fit was evaluated by calculating r^2 *values* and only fits with r^2 >0.80 were retained for further analyses (representing on average 80% of the acquired force-curves). The calculated values for elasticities are presented as mean value and standard deviation (Mean±SD).

Gene-set enrichment analysis (GSEA)

Data files containing the array data of the NF, HpAF, AdAF and CAF progression series are available at the NCBI Gene Expression Omnibus (GEO) under GSE45256. Array data was processed and analyzed using the Gene-set enrichment analysis software, developed by the Broad Institute of MIT and Harvard (USA) and available at www.broadinstitute.org, following the program guidelines. The specific settings applied in all analyses are: Number of Permutations (1000), Permutation Type (Gene set), Enrichment statistic (Weighted), Metric for ranking genes (*t* Test). The rest of the fields were left as defaulted. Gene sets were sourced from the Broad Institute database.

GSEA was used to interrogate the expression data on the expression of YAP target genes (*Cyr61, Amotl2, Ankrd1 and Ctgf*) to generate a heat map of expression.

Image analysis

Unless stated otherwise, image analysis was performed with Volocity (PerkinElmer). Spearman and Persons correlations were used to measure co-localization coefficients. To measure 'F-actin Stress Fiber Component' and 'Association of pMLC2 to Stress Fibers', 'non-cortical' and 'cortical' F-actin/pMLC2 intensities of individual cells were calculated and divided to generate a ratio of 'non-cortical' vs 'cortical' intensities that was used in the plots. To determine 'non-cortical' and 'cortical' regions, firstly the total area of the cell was delimited using F-actin staining, and total F-actin and pMLC2 intensities calculated after thresholding to reduce background signal. Total area was then cropped in to exclude the 'cortical' region, and the 'non-cortical' F-actin and pMLC2 intensities calculated. 'Cortical' F-actin and pMLC2 intensities were then calculated by subtracting the 'non-cortical' values from the total. To measure SEPT2 and SEPT7 fibrillar content, single cell SEPT2 and SEPT7 staining was thresholded to eliminate cytosolic background signal and the intersect of the resulting SEPT2 and SEPT7 areas used as the 'Fibrillar Septin Area'. To quantify focal adhesions, paxillin staining was thresholded to eliminate background signal and the resulting paxillin-positive area calculated. Plots represent the ratio of the paxillin-positive area to the total cellular area (determined by F-actin staining). To quantify YAP localization, a measure of its activation, nuclear YAP intensity (determined by the intensity within the region delimited by DAPI staining) and cytosolic YAP intensity (determined by the intensity without the region delimited by DAPI staining and within the region delimited by F-actin staining) were calculated. Plots represent the ratio of nuclear versus cytosolic YAP. To calculate the collagenase activity of CAFs, the mean intensity of FITC signal generated by cleaved ^{DQ}FITC-Col was calculated for each field of view containing an individual cell.

Figure S1

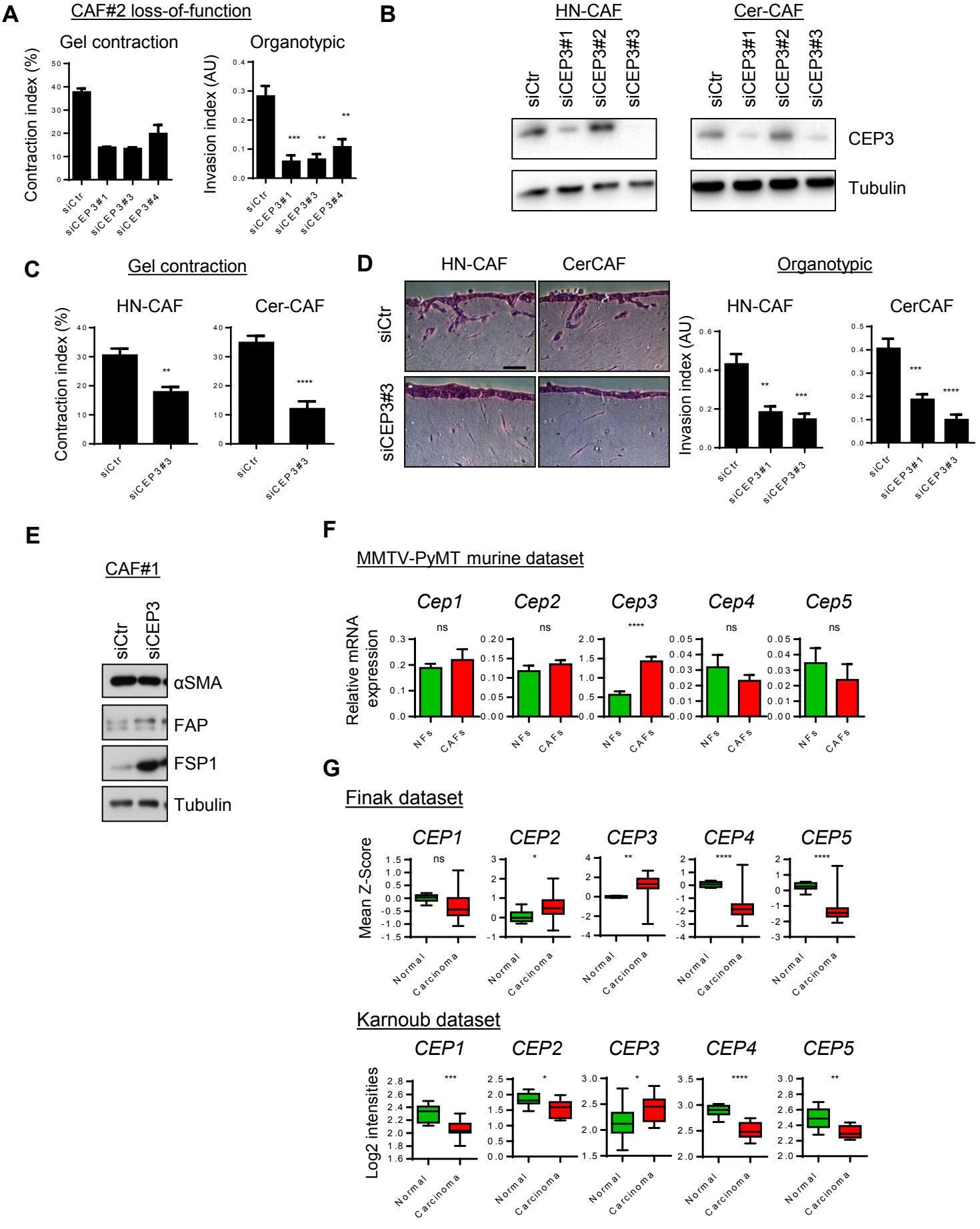
A
CAF#2 loss-of-function
Gel contraction
Organotypic
Contraction index (%)
Invasion index (AU)
siCtr
siCEP3#1
siCEP3#3
siCEP3#4
B
HN-CAF
Cer-CAF
siCtr
siCEP3#1
siCEP3#2
siCEP3#3
CEP3
Tubulin
C
Gel contraction
HN-CAF
Cer-CAF
Contraction index (%)
siCtr
siCEP3#3
D
HN-CAF
CerCAF
siCtr
siCEP3#3
Organotypic
Invasion index (AU)
siCEP3#1
E
CAF#1
siCtr
siCEP3
αSMA
FAP
FSP1
Tubulin
F
MMTV-PyMT murine dataset
Cep1
Cep2
Cep3
Cep4
Cep5
Relative mRNA expression
ns
NFs
CAFs
G
Finak dataset
CEP1
CEP2
CEP3
CEP4
CEP5
Mean Z-Score
Normal
Carcinoma
Karnoub dataset
Log2 intensities

Figure S1. Identification of Cdc42EP3 as a key regulator of CAF functions, related to Figure 1. (A) Quantification of gel contraction (left) and 4T1 organotypic invasion (right) of CAF#2 following transfection with control or three single Cdc42EP3 (CEP3) siRNA. Bars represent mean ± SEM (n=2 for gel contraction; n=10 organotypic assays assessed over 3 experiments). **(B)** Western blot showing Cdc42EP3 and tubulin expression in human CAFs from head-and-neck (HN-CAF) and cervical (Cer-CAF) carcinomas after transfection with control and 3 different Cdc42EP3 siRNA (siCEP3). **(C)** Histograms show gel contraction by HN-CAF and Cer-CAF following transfection with control or Cdc42EP3 siRNA (siCEP3#3). Bars represent mean ± SEM (n=7). **(D)** Representative images and quantification of SCC12 organotypic invasion of HN-CAF and Cer-CAF after transfection with control or Cdc42EP3 siRNAs. Bars represent mean ± SEM (n=5 organotypic assays assessed in one experiment). Scale bar, 100µm. **(E)** Representative Western blots showing αSMA, FAP, FSP1 and tubulin expression in CAF#1 following transfection with control or Cdc42EP3 siRNA (smart-pool). **(F)** Relative mRNA expression of BORG genes *Cdc42ep1* (*Cep1*), *Cdc42ep2* (*Cep2*), *Cdc42ep3* (*Cep3*), *Cdc42ep4* (Cep4) and *Cdc42ep5* (*Cep5*) in fibroblasts from normal murine mammary glands (NFs) and from MMTV-PyMT mammary carcinomas (CAFs). Bars represent the mean ± SEM of 4 different sets of NF (NF#1-4) and CAFs (CAF#1-4) performed on duplicate. **(G)** Box-and-whisker plots showing the relative expression of BORG genes *CDC42EP1* (*CEP1*), *CDC42EP2* (*CEP2*), *CDC42EP3* (*CEP3*), *CDC42EP4* (CEP4) and *CDC42EP5* (*CEP5*) in the stromal compartment of normal mammary glands or breast carcinoma in human disease. Plots were generated by interrogating the Finak Breast Dataset GSE9014 and Karnoub Breast Dataset GSE8977. The central box represents values from the lower to upper quartile. The middle line represents the mean. The horizontal line extends from the minimum to the maximum value.

Figure S2

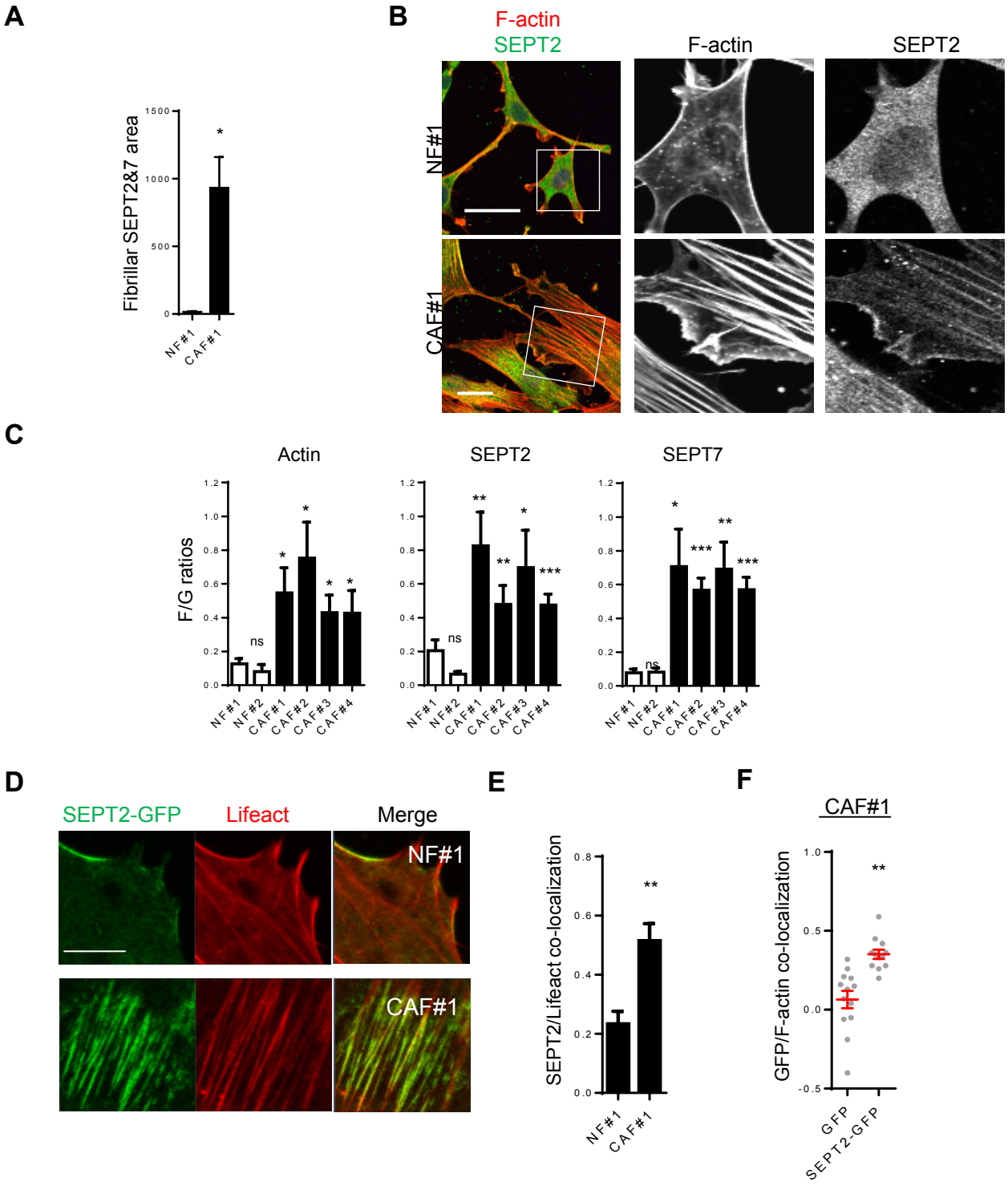

Supplementary Figure 2. CAFs have enhanced actin and septin cytoskeletal networks, related to Figure 2. (A) *From Figure 2A.* Histogram shows quantification of fibrillar SEPT2&7 in NF#1 and CAF#1. Bars represent mean ± SEM (n=5 for NF#1 and n=12 for CAF#1). **(B)** Representative images of NF#1 and CAF#1 fixed in 4% PFA and stained for F-actin (red) and SEPT2 (green). Indicated zoom up areas are shown in greyscale for each channel and cell type. Bars are 20µm. **(C)** *From Figure 2B.* Histograms show the F/G ratios of actin, SEPT2 and SEPT7. Bars represent mean ± SEM (n=6 for actin and SEPT2, n=4 for SEPT7). **(D)** Panels show stills from time-lapse movies S1 and S2 of SEPT2-GFP and MARS-Lifeact in NF#1 and CAF#1. **(E)** Histogram shows Spearman correlation co-efficient of co-localization of SEPT2-GFP and MARS-Lifeact signal in NF#1 and CAF#1. Bars represent mean ± SEM (n=10 cells). **(F)** Histogram shows Spearman correlation co-efficient of co-localization of GFP signal and F-actin in CAF#1 transfected with GFP or SEPT2-GFP. Line and error bars indicate mean ± SEM (n=12).

Figure S3

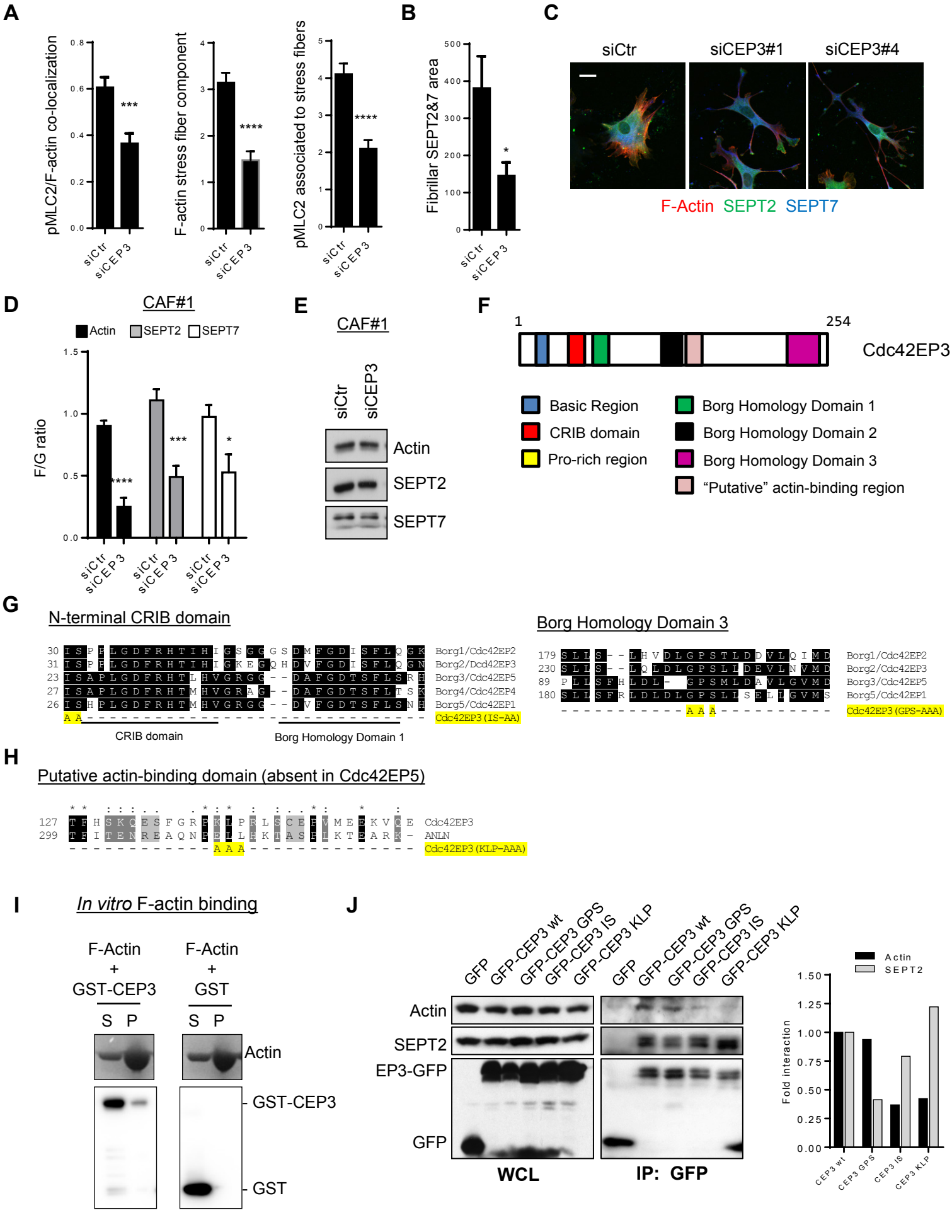
A
pMLC2/F-actin co-localization
F-actin stress fiber component
pMLC2 associated to stress fibers
siCtr
siCEP3
B
Fibrillar SEPT2&7 area
C
siCtr
siCEP3#1
siCEP3#4
F-Actin SEPT2 SEPT7
D
CAF#1
Actin
SEPT2
SEPT7
F/G ratio
E
CAF#1
siCtr
siCEP3
Actin
SEPT2
SEPT7
F
1
254
Cdc42EP3
Basic Region
CRIB domain
Pro-rich region
Borg Homology Domain 1
Borg Homology Domain 2
Borg Homology Domain 3
"Putative" actin-binding region
G
N-terminal CRIB domain
Borg1/Cdc42EP2
Borg2/Dcd42EP3
Borg3/Cdc42EP5
Borg4/Cdc42EP4
Borg5/Cdc42EP1
Cdc42EP3 (IS-AA)
CRIB domain
Borg Homology Domain 1
Borg Homology Domain 3
Cdc42EP3 (GPS-AAA)
H
Putative actin-binding domain (absent in Cdc42EP5)
Cdc42EP3
ANLN
Cdc42EP3 (KLP-AAA)
I
In vitro F-actin binding
F-Actin + GST-CEP3
F-Actin + GST
S P
Actin
GST-CEP3
GST
J
GFP
GFP-CEP3 wt
GFP-CEP3 GPS
GFP-CEP3 IS
GFP-CEP3 KLP
Actin
SEPT2
EP3-GFP
GFP
WCL
IP: GFP
Fold interaction
CEP3 wt
CEP3 GPS
CEP3 IS
CEP3 KLP

Figure S3. Cdc42EP3 regulates the actin and septin fibrillar networks, related to Figure 3. (A) *From Figure 3A.* Histograms show: Pearson correlation co-efficient of co-localization of pMLC2 and F-actin (left panel), F-actin stress fibers component (middle panel) and pMLC2 associated to stress fibers (right panel) of CAF#1 cells following transfection with control or Cdc42EP3 siRNA (siCEP3, smart-pool). Bars represent mean ± SEM (n=10 single cell measurements). **(B)** *From Figure 3B.* Histogram shows fibrillar SEPT2&7 of CAF#1 cells following transfection with control or Cdc42EP3 siRNA (siCEP3, smart-pool). Bars represent mean ± SEM (n=23 single cell measurements). **(C)** Representative images of CAF#1 transfected with control or two independent Cdc42EP3 siRNA, fixed in 4% PFA and stained for F-actin (red), SEPT2 (green) and SEPT7 (red). Bars are 20µm. **(D)** *From Figure 3C.* Histogram shows the F/G ratios of actin, SEPT2 and SEPT7 of CAF#1 following transfection with control and Cdc42EP3 siRNA (siCEP3 smart-pool). Bars represent mean ± SEM (n=7). **(E)** Representative Western blots showing actin, SEPT2 and SEPT7 expression in CAF#1 following transfection with control or Cdc42EP3 siRNA (smart-pool). **(F)** Diagram showing the different domains and functional regions in murine Cdc42EP3 (254 aa). **(G)** Sequence alignments of Cdc42EP2, Cdc42EP3, Cdc42EP5, Cdc42EP4 and Cdc42EP1 in the N-terminal regions (containing the CRIB domain and Borg Homology Domain 1/BHD1), and BHD3 domain regions. Conserved residues are highlighted in black. Mutated residues in the Cdc42EP3 mutants IS-AA and GPS-AAA are highlighted in yellow. **(H)** Alignments of Cdc42EP3 with ANLN and Villin showing the putative actin-binding region present in Cdc42EP3 but absent in Cdc42EP5. Conserved residues are highlighted in black, whereas semi-conserved residues are in two different degrees of grey. Mutated residues in the Cdc42EP3 mutant KLP-AAA are highlighted in yellow. **(I)** Coomassie-stained gel (actin) and western blots (anti-GST) showing equal volumes of supernatant (S) and pellet (P) fractions from high-speed sedimentation of pre-polymerized actin filaments in the presence of recombinant GST-Cdc42EP3 or GST. **(J)** Western blots show anti-GFP co-immune-precipitation of actin and SEPT2 with over-expressed GFP or Cdc42EP3-GFP proteins in HEK293 cells. Wild-type (wt), and Cdc42EP3 (CEP3) mutants IS-AA, GPS-AAA and KLP-AAA are shown. Graph represents quantification of the blots indicating the amount of Actin and SEPT2 bound to Cdc42EP3 mutants relative to Cdc42EP3 wild-type.

Figure S4. Calvo et al

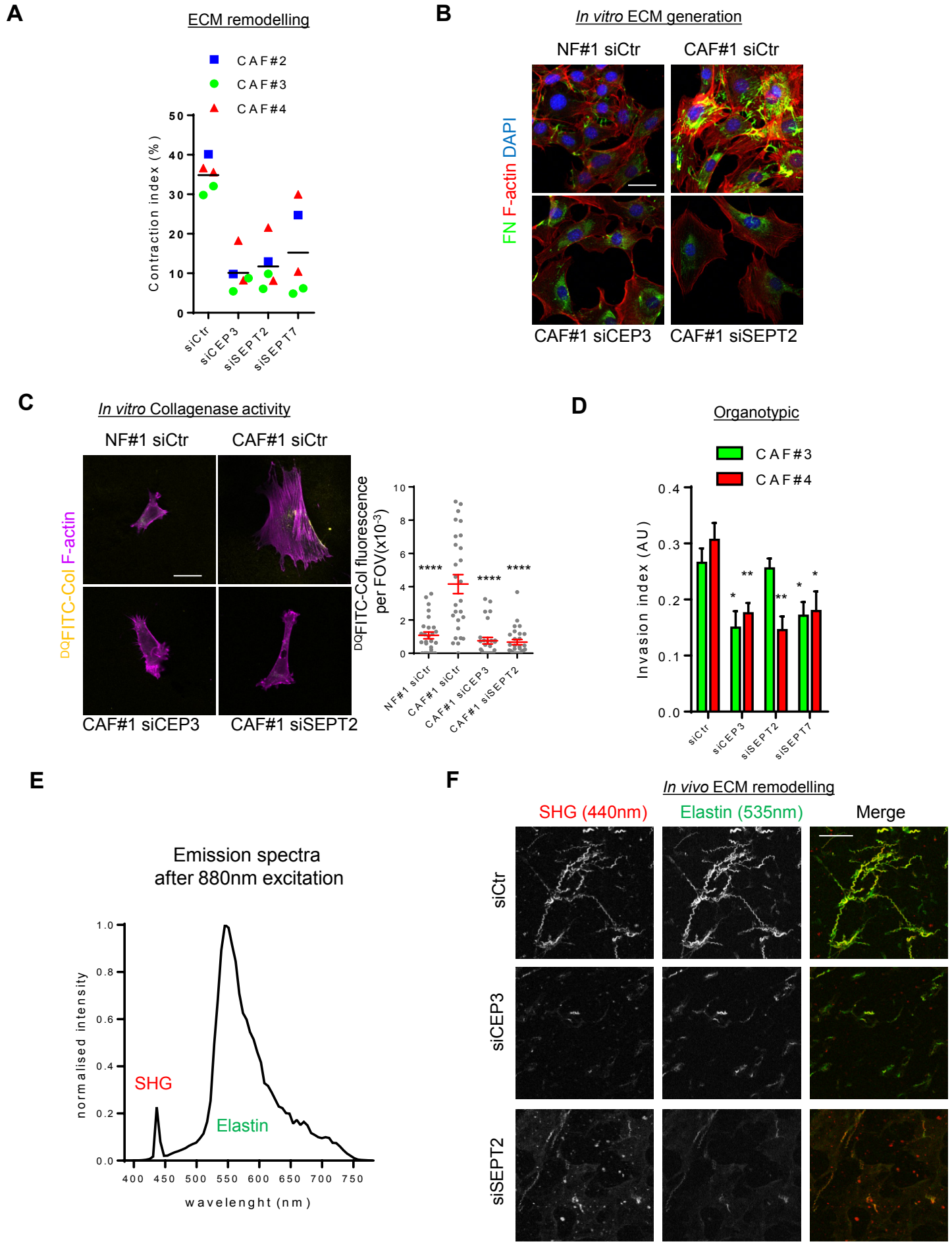

Figure S4. The septin cytoskeleton is required for CAF functions., related to Figure 4. (A) Histogram shows gel contraction by CAF#2 (blue), CAF#3 (green) and CAF#4 (red) following transfection with control, Cdc42EP3 (CEP3), SEPT2 and SEPT7 siRNA. Every experiment is shown individually. Lines represent mean of all cell lines. **(B)** Images show merged channels of fibronectin (FN, green), F-actin (red) and DAPI (blue) staining of NF#1 and CAF#1 following transfection with control, Cdc42EP3 (siCEP3) and SEPT2 siRNAs (smart-pools). **(C)** Images show merged channels of cleaved collagen (^{DQ}FITC-Col, yellow) and F-actin (red) staining of NF#1 and CAF#1 following transfection with control, Cdc42EP3 (CEP3) and SEPT2 siRNAs (smart-pools). Histogram shows ^{DQ}FITC-Col fluorescence area per single cell of the indicated experimental points. Line and error bars indicate mean ± SEM (n=27 individual cells). **(D)** Quantification of 4T1 invasion when co-cultured with CAF#3 (green) and CAF#4 (red) following transfection with control, Cdc42EP3 (CEP3), SEPT2 and SEPT7 siRNA. Bars represent mean ± SEM (n=4). **(E)** Emission spectral un-mixing of CAF matrix plugs. Chart shows normalized intensity of emitted light at the indicated wavelengths of CAF matrix plug samples after excitation with an 880 nm pulsed Ti–Sapphire laser. Peak at 440nm corresponds to the second harmonic generation (SHG) signal from collagen fibers and the second peak comes from elastin autofluorescence. **(F)** Panels show second harmonic generation (SHG) of collagen fibers (red) and elastin autofluorescent signal (green) of CAF#1 matrix plugs transfected with control, Cdc42EP3 (CEP3) and SEPT2 siRNA (smart-pools). Each channel is also shown individually in greyscale. Scale bar, 30μm.

Figure S5

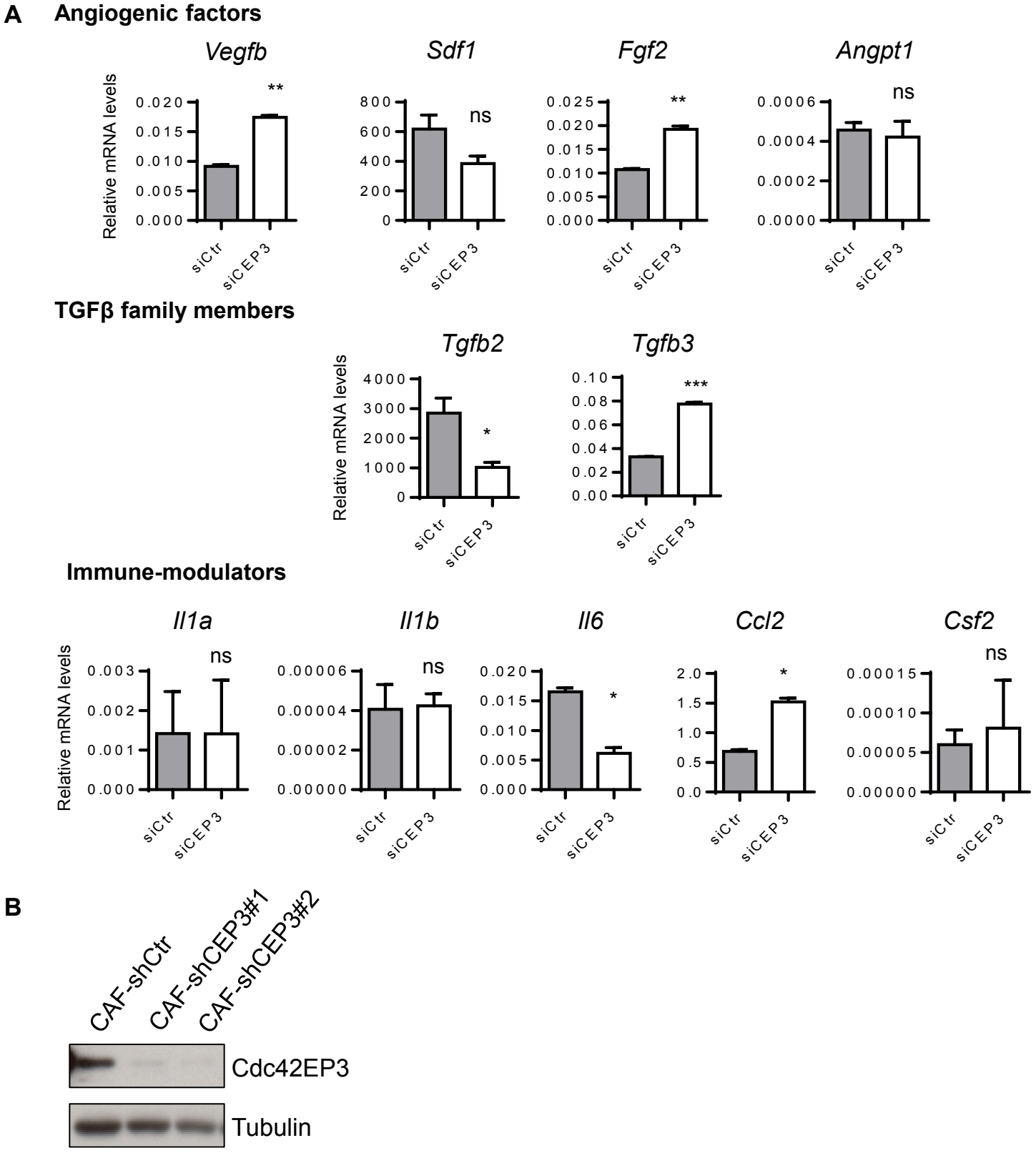

Figure S5. Cdc42EP3 is required for the pro-tumorigenic activity of CAFs *in vivo*, related to Figure 5. (A) Relative mRNA levels of angiogenic factors (*Vegfb*, *Sdf1/Cxcl12*, *Fgf2*, *Angpt1*), TGFβ family members (*Tgfb2* and *Tgfb3*) and immune-modulator (*Il1a*, *Il1b* and *Il6*, *Ccl2* and *Csf2*) in CAF#1 following transfection with control and Cdc42EP3 siRNA (CEP3, smart-pool). Bars represent mean ± SEM (n=3). **(B)** Western blot showing Cdc42EP3 and tubulin expression in CAF#3 after stable transfection with control and 2 different Cdc42EP3 shRNA (shCEP3).

Figure S6

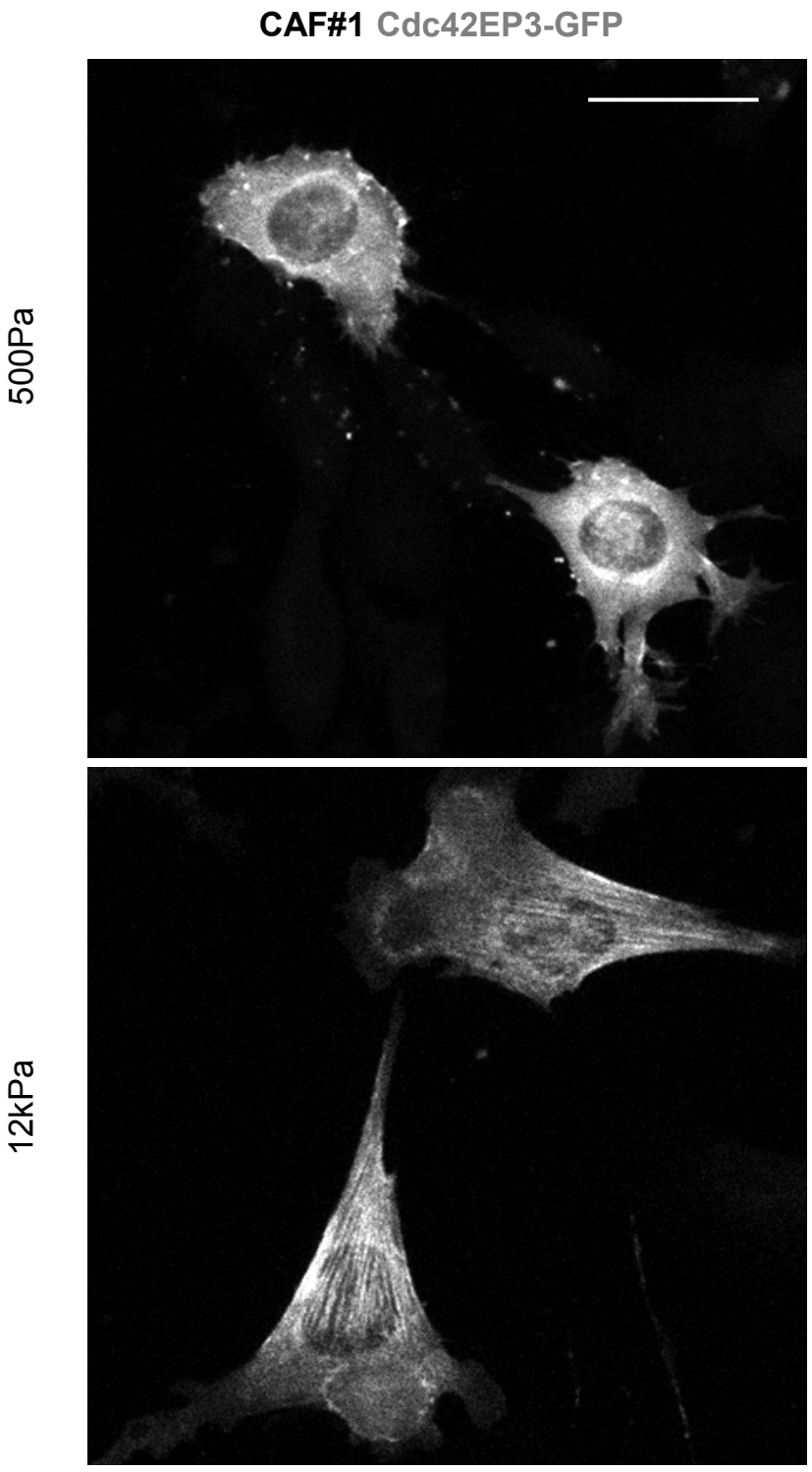

Figure S6. Cdc42EP3 is required for mechano-sensing, related to Figure 6. Images show GFP signal (greyscale) of Cdc42EP3-GFP-tranfected CAF#1 when seeded on soft (~500 Pa) and stiff (~12 kPa) matrices. Scale bar is 50μm.

Figure S7

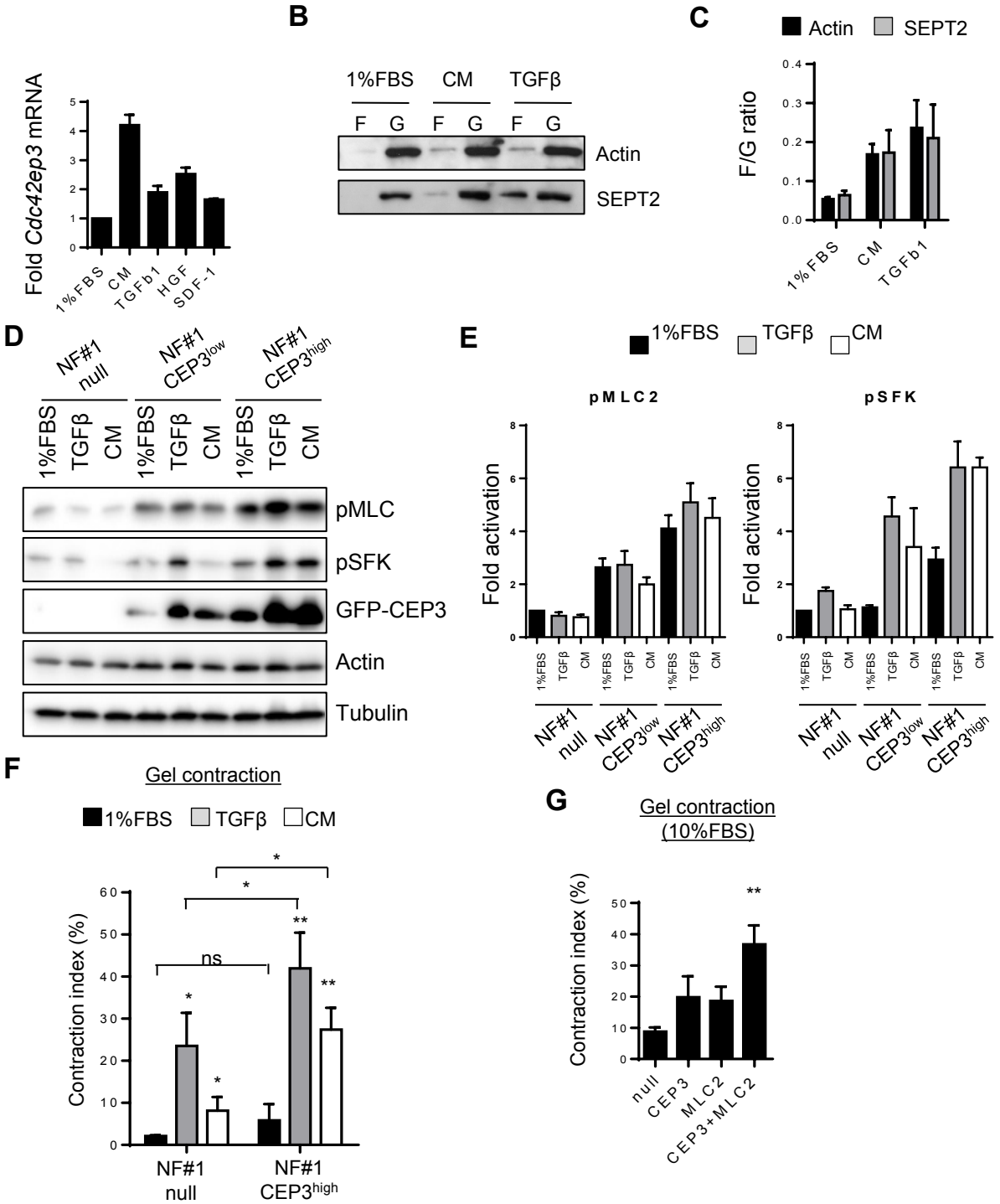

Figure S7. Cdc42EP3 is induced and required early in fibroblast activation, related to Figure 7. (A) Fold mRNA expression levels of *Cdc42ep3* in NF#1 subjected to 1%FBS, breast cancer cell conditioned media (CM), 2 ng/mL of TGFβ, 5 ng/mL of HGF or 50 ng/mL SDF-1 for 6 hours. Bars represent mean ± SEM (n=6). **(B)** Western blots showing fibrillar (F) and soluble (G) actin and SEPT2 levels in NF#1 subjected to 1% FBS, breast cancer cell conditioned media (CM) or 2 ng/mL of TGFβ for 3 days. **(C)** Histogram shows the F/G ratios of actin and SEPT2. Bars represent mean ± SEM (n=3). **(D)** Representative Western blots showing actin, tubulin, GFP (CEP3) and phosphorylated levels of pS19-MLC2 (pMLC2), pY118-paxillin (pPax) and pY416-Src (pSFK) in stable cell lines NF#1-null, NF#1-Cdc42EP3^{low} and NF#1-Cdc42EP3^{high} following stimulation with 1%FBS, 2ng/mL TGFβ and breast cancer cell conditioned media (CM) for 16h. **(E)** Charts show the fold levels of pMLC2, pPax and pSFK (n=4). **(F)** Histogram shows gel contraction by stable cell lines NF#1-null and NF#1-Cdc42EP3^{high} under stimulation with 1%FBS, 2ng/mL TGFβ and breast cancer cell conditioned media (CM). Bars represent mean ± SEM (n=3). **(G)** Histogram shows the gel contraction of NF#1 following transfection with empty vector (null), Cdc42EP3 (CEP3), MLC2 or Cdc42EP3 & MLC2. Bars represent mean ± SEM (n=4).

Supplementary Tables

Table S1. siRNAs used in this study, related to Experimental Procedures

siRNA	Company	Cat. No	Species
Cdc42EP3 oligo 1	Dharmacon	D-046421-01	Mouse
Cdc42EP3 oligo 2	Dharmacon	D-046421-02	Mouse
Cdc42EP3 oligo 3	Dharmacon	D-046421-03	Mouse
Cdc42EP3 oligo 4	Dharmacon	D-046421-04	Mouse
ANLN oligo 1	Dharmacon	D-056109-01	Mouse
ANLN oligo 2	Dharmacon	D-056109-02	Mouse
ANLN oligo 3	Dharmacon	D-056109-03	Mouse
ANLN oligo 4	Dharmacon	D-056109-04	Mouse
SEPT2 oligo 1	Dharmacon	D-051534-01	Mouse
SEPT2 oligo 2	Dharmacon	D-051534-02	Mouse
SEPT2 oligo 3	Dharmacon	D-051534-03	Mouse
SEPT2 oligo 4	Dharmacon	D-051534-04	Mouse
SEPT7 oligo 1	Dharmacon	D-042160-01	Mouse
SEPT7 oligo 2	Dharmacon	D-042160-02	Mouse
SEPT7 oligo 3	Dharmacon	D-042160-03	Mouse
SEPT7 oligo 4	Dharmacon	D-042160-04	Mouse
DIAPH3 oligo 1	Dharmacon	D-049507-01	Mouse
DIAPH3 oligo 2	Dharmacon	D-049507-02	Mouse
DIAPH3 oligo 3	Dharmacon	D-049507-03	Mouse
DIAPH3 oligo 4	Dharmacon	D-049507-04	Mouse
TAGLN oligo 1	Dharmacon	D-062786-01	Mouse
TAGLN oligo 2	Dharmacon	D-062786-02	Mouse
TAGLN oligo 3	Dharmacon	D-062786-03	Mouse
TAGLN oligo 4	Dharmacon	D-062786-04	Mouse
THBS1 oligo 1	Dharmacon	D-044041-01	Mouse
THBS1 oligo 2	Dharmacon	D-044041-02	Mouse
THBS1 oligo 3	Dharmacon	D-044041-03	Mouse
THBS1 oligo 4	Dharmacon	D-044041-04	Mouse
DIAPH1 oligo 1	Dharmacon	d-064854-05	Mouse
DIAPH1 oligo 2	Dharmacon	d-064854-06	Mouse
DIAPH1 oligo 3	Dharmacon	d-064854-07	Mouse
DIAPH1 oligo 4	Dharmacon	d-064854-08	Mouse
PDLIM4 oligo 1	Dharmacon	D-056154-01	Mouse
PDLIM4 oligo 2	Dharmacon	D-056154-02	Mouse
PDLIM4 oligo 3	Dharmacon	D-056154-03	Mouse
PDLIM4 oligo 4	Dharmacon	D-056154-04	Mouse
ARHGAP18 oligo 1	Dharmacon	D-057063-01	Mouse
ARHGAP18 oligo 2	Dharmacon	D-057063-02	Mouse
ARHGAP18 oligo 3	Dharmacon	D-057063-03	Mouse
ARHGAP18 oligo 4	Dharmacon	D-057063-04	Mouse
ARHGDIB oligo 1	Dharmacon	D-042404-01	Mouse
ARHGDIB oligo 2	Dharmacon	D-042404-02	Mouse
ARHGDIB oligo 3	Dharmacon	D-042404-03	Mouse
ARHGDIB oligo 4	Dharmacon	D-042404-04	Mouse
SDC3 oligo 1	Dharmacon	D-059803-01	Mouse
SDC3 oligo 2	Dharmacon	D-059803-02	Mouse
SDC3 oligo 3	Dharmacon	D-059803-03	Mouse
SDC3 oligo 4	Dharmacon	D-059803-04	Mouse
SDC1 oligo 1	Dharmacon	D-044225-01	Mouse
SDC1 oligo 2	Dharmacon	D-044225-02	Mouse
SDC1 oligo 3	Dharmacon	D-044225-03	Mouse
SDC1 oligo 4	Dharmacon	D-044225-04	Mouse

SDC2 oligo 1	Dharmacon	D-046419-01	Mouse
SDC2 oligo 2	Dharmacon	D-046419-02	Mouse
SDC2 oligo 3	Dharmacon	D-046419-03	Mouse
SDC2 oligo 4	Dharmacon	D-046419-04	Mouse
SDC4 oligo1	Dharmacon	D-044221-01	Mouse
SDC4 oligo2	Dharmacon	D-044221-02	Mouse
SDC4 oligo3	Dharmacon	D-044221-03	Mouse
SDC4 oligo4	Dharmacon	D-044221-04	Mouse
DSTN oligo 1	Dharmacon	D-049526-01	Mouse
DSTN oligo 2	Dharmacon	D-049526-02	Mouse
DSTN oligo 3	Dharmacon	D-049526-03	Mouse
DSTN oligo 4	Dharmacon	D-049526-04	Mouse
NES oligo 1	Dharmacon	D-057300-01	Mouse
NES oligo 2	Dharmacon	D-057300-03	Mouse
NES oligo 3	Dharmacon	D-057300-04	Mouse
NES oligo 4	Dharmacon	D-057300-17	Mouse
SDCBP oligo 1	Dharmacon	D-043821-01	Mouse
SDCBP oligo 2	Dharmacon	D-043821-02	Mouse
SDCBP oligo 3	Dharmacon	D-043821-03	Mouse
SDCBP oligo 4	Dharmacon	D-043821-04	Mouse
TACC1 oligo 1	Dharmacon	D-050702-01	Mouse
TACC1 oligo 2	Dharmacon	D-050702-02	Mouse
TACC1 oligo 3	Dharmacon	D-050702-03	Mouse
TACC1 oligo 4	Dharmacon	D-050702-04	Mouse
AGTR1 oligo 1	Dharmacon	D-057103-01	Mouse
AGTR1 oligo 2	Dharmacon	D-057103-02	Mouse
AGTR1 oligo 3	Dharmacon	D-057103-03	Mouse
AGTR1 oligo 4	Dharmacon	D-057103-04	Mouse
GEF-H1 (AHRGEF2) oligo1	Dharmacon	D-040120-01	Mouse
GEF-H1 (AHRGEF2) oligo2	Dharmacon	D-040120-02	Mouse
GEF-H1 (AHRGEF2) oligo3	Dharmacon	D-040120-03	Mouse
GEF-H1 (AHRGEF2) oligo4	Dharmacon	D-040120-04	Mouse
LARG (ARHGEF12) oligo1	Dharmacon	D-041056-01	Mouse
LARG (ARHGEF12) oligo2	Dharmacon	D-041056-02	Mouse
LARG (ARHGEF12) oligo3	Dharmacon	D-041056-03	Mouse
LARG (ARHGEF12) oligo4	Dharmacon	D-041056-04	Mouse
ROCK1 oligo1	Dharmacon	D-046504-01	Mouse
ROCK1 oligo2	Dharmacon	D-046504-02	Mouse
ROCK1 oligo3	Dharmacon	D-046504-03	Mouse
ROCK1 oligo4	Dharmacon	D-046504-04	Mouse
RHOG oligo1	Dharmacon	D-064124-01	Mouse
RHOG oligo2	Dharmacon	D-064124-02	Mouse
RHOG oligo3	Dharmacon	D-064124-03	Mouse
RHOG oligo4	Dharmacon	D-064124-04	Mouse
Ifi27l2a oligo 1	Dharmacon	D-063667-01	Mouse
Ifi27l2a oligo 2	Dharmacon	D-063667-02	Mouse
Ifi27l2a oligo 3	Dharmacon	D-063667-03	Mouse
Ifi27l2a oligo 4	Dharmacon	D-063667-04	Mouse
Cdc42EP3 oligo 1	Dharmacon	D-017358-01	Human
Cdc42EP3 oligo 2	Dharmacon	D-017358-02	Human
Cdc42EP3 oligo 3	Dharmacon	D-017358-03	Human
Cdc42EP3 oligo 4	Dharmacon	D-017358-04	Human

Table S2. Antibodies used in this study, related to Experimental Procedures.

Antibody	Company	Cat. No	Clonal	Dilution			
				IF	WB	IHC	IP
14-3-3	Santa Cruz	1647	Monoclonal (H8)		1:1000		
Actin	Sigma	13853	monoclonal (Clone AC40)		1:1000		
Beta-Tubulin	Sigma	T7816	monoclonal (clone SAP.4G5)	1:100			
Cdc42EP3	proteintech	10780	polyclonal	1:100	1:500		
Cdc42EP5	Abcam	ab75004	polyclonal		1:500		
Endomucin	Santa cruz	65495	monoclonal (clone V.7C7)			1:200	
GFP	Santa cruz	8334	polyclonal		1:1000		1:200
GFP	Roche	11814460 001	monoclonal (clones 7.1 and 13.1)		1:5000		1:200
GST	GE Healthcare	27-4577-01	Polyclonal		1:1000		
Paxillin	Transduction labs	610051	monoclonal (clone 349)	1:100			
Phalloidin-TRITC	Sigma	P1951	n/a	1:500			
Phospho-MLC2 (S19)	Cell Signaling	3672	polyclonal	1:100	1:1000		
Phospho-Paxilin (Y118)	Invitrogen	44-722G	Polyclonal		1:1000		
Phospho-Src Family Kinases (Y416)	Cell Signaling	2101	polyclonal		1:1000		
SEPT2	proteintech	60075	monoclonal (ag1946)	1:100	1:1000		
SEPT7	proteintech	13818	polyclonal	1:100	1:1000		
Vimentin	Sigma	V2258	monoclonal (clone LN-6)	1:500		1:250	
YAP	Santa cruz	101199	monoclonal (clone 63.7)	1:200	1:2000		1:100

Table S3. Oligonucleotides used in this study, related to Experimental Procedures.

Target		Sequence	Target full name	species
Amolt2	F	AACCGCCACCTGGCAAGCAA	Angiomotin like 2	mouse
	R	GGTCCTCGATGGCACCACGC		mouse
Angpt1	F	CACATAGGGTGCAGCAACCA	Angiopoietin 1	mouse
	R	CGTCGTGTTCTGGAAGAATGA		mouse
Ankrd1	F	AAACGGACGGCACTCCACCG	Ankyrin repeat domain 1	mouse
	R	CGCTGTGCTGAGAAGCTTGTCTCT		mouse
Ccl2	F	TTAAAAACCTGGATCGGAACCAA	Chemokine (C-C motif) ligand 2	mouse
	R	GCATTAGCTTCAGATTTACGGGT		mouse
Cdc42ep1	F	ATGTCTTCGGAGATACGTCCTT	Cdc42 effector protein 1 (Cdc42EP1)	mouse
	R	GACTCTGCGAACCTGTTGGA		mouse
Cdc42ep2	F	TCCCCATCTATTTGAAACGTGG	Cdc42 effector protein 2 (Cdc42EP2)	mouse
	R	CCGCTGTTCCTGGAAGGAG		mouse
Cdc42ep3	F	AACACCCTCCCCGGTGCTCAA	Cdc42 effector protein 3 (Cdc42EP3)	mouse
	R	CTCCCTGGTGGACTGCCCCAT		mouse
Cdc42ep4	F	CAGCTCTGTGAACTCGAAGC	Cdc42 effector protein 4 (Cdc42EP4)	mouse
	R	GCTAGTGAGGAAAGACGTGTCC		mouse
Cdc42ep5	F	GGGATGCCCACCCTAGAGT	Cdc42 effector protein 5 (Cdc42EP5)	mouse
	R	TGGAGGTCAGCATTTGAGCAG		mouse
Csf2	F	GGCCTTGGAAGCATGTAGAGG	Colony stimulating factor 2 (granulocyte-macrophage) / GM-CSF	mouse
	R	GGAGAACTCGTTAGAGACGACTT		mouse
Ctgf	F	CCCTGCCCTAGCTGCCTACCG	Connective tissue growth factor	mouse
	R	GCTTCGCAGGGCCTGACCAT		mouse
Cyr61	F	GCCGTGGGCTGCATTCCTCT	Cysteine-rich angiogenic induce 61	mouse
	R	GCGGTTCGGTGCCAAAGACAGG		mouse
Fgf2	F	GCGACCCACACGTCAAACTA	Fibroblast growth factor 2	mouse
	R	TCCCTTGATAGACACAACTCCTC		mouse
Il1a	F	CGAAGACTACAGTTCTGCCATT	Interleukin 1 alpha	mouse
	R	GACGTTTCAGAGGTTCTCAGAG		mouse
Il1b	F	GAAATGCCACCTTTTGACAGTG	Interleukin 1 beta	mouse
	R	TGGATGCTCTCATCAGGACAG		mouse
Il6	F	TAGTCCTTCCTACCCCAATTTCC	Interleukin 6	mouse
	R	TTGGTCCTTAGCCACTCCTTC		mouse
Lamc2	F	ATGGGTCTCCTGCAAAGCTC	Laminin, gamma 2	mouse
	R	AAAGTAACTCAGCTGGGGGC		mouse
Rplp1	F	ACCGTGCCGGCAGTCTACAG	Ribosomal Protein Large, P1	mouse
	R	ATGTTGACATTGGCCAGAGCCTTG		mouse
Sdf1	F	TGCATCAGTGACGGTAAACCA	Chemokine (C-X-C motif) ligand 12 / CXCL12	mouse
	R	TTCTTCAGCCGTGCAACAATC		mouse

Tgfb1	F	CTCCCGTGGCTTCTAGTGC	Transforming growth factor, beta 1	mouse
	R	GCCTTAGTTTGGACAGGATCTG		mouse
Tgfb2	F	TCGACATGGATCAGTTTATGCG	Transforming growth factor, beta 2	mouse
	R	CCCTGGTACTGTTGTAGATGGA		mouse
Tgfb3	F	CCTGGCCCTGCTGAACTTG	Transforming growth factor, beta 3	mouse
	R	TTGATGTGGCCGAAGTCCAAC		mouse
Vegfa	F	GCACATAGAGAGAATGAGCTTCC	Vascular endothelial growth factor A	mouse
	R	CTCCGCTCTGAACAAGGCT		mouse
Vegfc	F	GAGGTCAAGGCTTTTGAAGGC	Vascular endothelial growth factor C	mouse
	R	CTGTCCTGGTATTGAGGGTGG		mouse